

TECHNICAL ADVANCE

Metabolomic profiling of wild-type and mutant soybean root nodules using laser-ablation electrospray ionization mass spectrometry reveals altered metabolism

Beverly J. Agtuca¹ , Sylwia A. Stopka² , Sterling Evans¹ , Laith Samarah² , Yang Liu³, Dong Xu³, Minviluz G. Stacey¹ , David W. Koppenaal⁴, Ljiljana Paša-Tolić⁴, Christopher R. Anderton⁴ , Akos Vertes²  and Gary Stacey^{1*} 

¹Divisions of Plant Sciences and Biochemistry, Christopher S. Bond Life Sciences Center, University of Missouri, Columbia, MO, 65211, USA,

²Department of Chemistry, The George Washington University, Washington, DC, 20052, USA,

³Department of Electrical Engineering and Computer Science, Informatics Institute and Christopher S. Bond Life Sciences Center, University of Missouri-Columbia, Columbia, MO, 65211, USA, and

⁴Environmental Molecular Sciences Laboratory, Earth and Biological Sciences Directorate, Pacific Northwest National Laboratory, 902 Battelle Boulevard, Richland, WA, 99354, USA

Received 19 June 2019; revised 5 April 2020; accepted 17 April 2020.

*For correspondence (e-mail: staceyg@missouri.edu).

SUMMARY

The establishment of the nitrogen-fixing symbiosis between soybean and *Bradyrhizobium japonicum* is a complex process. To document the changes in plant metabolism as a result of symbiosis, we utilized laser ablation electrospray ionization-mass spectrometry (LAESI-MS) for *in situ* metabolic profiling of wild-type nodules, nodules infected with a *B. japonicum nifH* mutant unable to fix nitrogen, nodules doubly infected by both strains, and nodules formed on plants mutated in the *stearoyl-acyl carrier protein desaturase (sacpd-c)* gene, which were previously shown to have an altered nodule ultrastructure. The results showed that the relative abundance of fatty acids, purines, and lipids was significantly changed in response to the symbiosis. The *nifH* mutant nodules had elevated levels of jasmonic acid, correlating with signs of nitrogen deprivation. Nodules resulting from the mixed inoculant displayed similar, overlapping metabolic distributions within the sectors of effective (*fix*⁺) and ineffective (*nifH* mutant, *fix*⁻) endosymbionts. These data are inconsistent with the notion that plant sanctioning is cell autonomous. Nodules lacking *sacpd-c* displayed an elevation of soyasaponins and organic acids in the central necrotic regions. The present study demonstrates the utility of LAESI-MS for high-throughput screening of plant phenotypes. Overall, nodules disrupted in the symbiosis were elevated in metabolites related to plant defense.

Keywords: LAESI-MS, nodulation, nitrogen fixation, metabolites, plant defense, *sacpd-c*, soybean, sanctions, high-throughput, mass spectrometry, technical advance.

INTRODUCTION

The nitrogen-fixing symbiosis between legumes and rhizobia provides approximately 40 million tons of nitrogen into agricultural systems each year (Oldroyd, 2013; Udvardi and Poole, 2013). This symbiotic relationship is ecologically beneficial because it improves soil health, diminishes the use of fossil fuels, and lessens the negative environmental effects resulting from agricultural practices (Hardy and Havelka, 1975; Udvardi and Poole, 2013; Vicente and Dean,

2017). Recently, there has been a resurgence of interest in the possibility of transferring the rhizobial, nitrogen-fixing symbiosis to non-legumes (e.g. corn) (Charpentier and Oldroyd, 2010; Beatty and Good, 2011). However, for this to become a practical possibility, a more in-depth understanding of the physiology of legume nodule formation and function is required.

The symbiotic interaction between the symbiont, *Bradyrhizobium japonicum*, and soybean roots involves a

complex communication process involving different signaling molecules crucial for the initiation and development of root nodules (Stacey, 2007; Oldroyd, 2013). The net result of this communication and coordination is the formation of a specialized organ, called a nodule, on the roots. Biological nitrogen fixation (BNF) takes place inside the nodules, where atmospheric dinitrogen is converted into ammonia, a nutrient form that can be metabolized by plants (Udvardi and Poole, 2013).

To determine the molecular mechanisms involved in nodulation, researchers have utilized transcriptomics and proteomics to identify and characterize genes and proteins critical for the symbiosis (Stacey *et al.*, 2006; Libault, 2018). Relatively few studies have explored the nodule metabolome. Although transcriptomics and proteomics are undoubtedly useful, they do not provide direct evidence that the genes and proteins detected are indeed metabolically active under the various conditions studied. On the other hand, metabolomic profiling provides a direct readout of the metabolism that is occurring. Most of the published studies of the nodule metabolome have used bulk methods, in which the nodules were extracted and the metabolites were measured. For example, studies have utilized technologies such as gas chromatography-mass spectrometry (MS), high-performance liquid chromatography-MS, and capillary electrophoresis-MS (Sato *et al.*, 1998; Soga *et al.*, 2003; Colebatch *et al.*, 2004; Desbrosses *et al.*, 2005; Barsch *et al.*, 2006a,b; Larrainzar *et al.*, 2007; Harada and Fukusaki, 2009; Brechenmacher *et al.*, 2010; Zhang *et al.*, 2012; Wang *et al.*, 2015). All of these approaches require extensive sample preparation that eliminates the possibility of also acquiring information on the spatial distribution of the various metabolites. Spatial information can be beneficial by, for example, allowing correlation between the distribution of metabolites produced in a single pathway or related pathways, such as hormonal pathways regulating plant growth. Acquiring information on the spatial distribution of metabolites requires the use of MS methods that are spatially explicit MS techniques. For example, matrix-assisted laser desorption/ionization (MALDI)-MS imaging (MSI) is a technique, most commonly performed under vacuum, for spatially mapping biomolecules (Veličković *et al.*, 2018). However, this method requires the application of an organic matrix resulting in spectral interference and it can suffer from a narrow dynamic range (Ye *et al.*, 2013; Gemperline *et al.*, 2015). Ambient, direct analysis MS methods, such as laser ablation electrospray ionization MS (LAESI-MS), are gaining popularity because of the ability to spatially probe biological tissues with minimal sample preparation. Briefly, LAESI-MS utilizes a mid-infrared laser that couples energy directly into the O-H vibrations of water molecules (Nemes and Vertes, 2007). Because plant cells have a high-water content, this technique is amenable to the direct analysis

of metabolites. Previously, we demonstrated the application of LAESI-MS for the direct analysis of soybean nodules infected by wild-type (WT) *B. japonicum* (Stopka *et al.*, 2017). In this study, known metabolites in the nodules were detected similarly to other bulk MS analyses; however, the LAESI-MS approach provided information on the spatial distribution of these metabolites.

To provide insight into the soybean symbiotic relationship, plant and bacterial mutants are key tools for the identification of metabolites required for the establishment and maintenance of symbiotic nitrogen fixation. For example, to study nodules that are unable to fix nitrogen (fix^-), a *B. japonicum* strain with a mutation in the *nifH* gene, which encodes the nitrogenase reductase enzyme (Hahn *et al.*, 1984), can be studied at the metabolic level. Under some circumstances, nodules can be simultaneously infected with two strains, localizing to distinct sectors. For example, some studies have looked closely at nodules infected simultaneously with effective (fix^+) and ineffective (fix^-) rhizobia. In this case, the white sectors infected by the fix^- strain can be distinguished from the red (as a result of leghemoglobin) sectors formed by the fix^+ strain. In a number of studies, the host plant is suggested to have the ability to 'sanction' nodules that are unable to fix nitrogen (or fix lower levels of nitrogen) (Denison, 2000; Kiers *et al.*, 2003). One example is the study by Regus *et al.* (2017), who looked specifically at nodules doubly infected by fix^- and fix^+ rhizobia. Their surprising conclusion, based largely on microscopy, was that the plant applied sanctions were cell autonomous and applied exclusively within the doubly infected nodules to those sectors infected by the fix^- rhizobia. Given that most plant responses to stress are systemic, this conclusion was surprising and, hence, in the present study, we examined the case of doubly infected nodules at a deeper level by examining the metabolome of the fix^- and fix^+ sectors.

In addition to examination of nodules resulting from infection by bacterial mutants, a variety of studies have also utilized plant mutants; for example, to help elucidate signaling steps involved in nodule initiation (Oldroyd, 2013). Previously, we showed that the infection of a soybean mutant defective in the *sacpd-c* gene not only resulted in nodules with reduced fixation ability, but also prominent necrotic areas in the center of the nodules (Gillman *et al.*, 2014). Subsequently, it was found that the *sacpd-c* mutant nodules also showed a significantly higher expression of genes usually associated with plant response to pathogen infection (Krishnan *et al.*, 2016). Hence, in the present study, we examined the metabolome of these *sacpd-c* mutant nodules to elucidate changes associated with the necrotic regions.

We employed LAESI-MS, as a result of its capability for *in situ* sampling of defined areas, for the rapid phenotypic screening of nodules that were unable to fix nitrogen, either because of mutations in the symbiont or the host. Three different mutants were analyzed: (i) nodules that

were infected by a *nifH* (fix^-) bacterial strain; (ii) nodules that were infected by a mixed inoculum [wild-type (fix^+) *B. japonicum* (WT) and *nifH* (fix^-) mutant strain]; and (iii) *sacpd-c* mutant nodules. Here, we present the specific metabolites and affected biochemical pathways based on these different symbiotic interactions.

RESULTS

Carbon and nitrogen metabolism detected in nitrogen-fixing soybean roots

In a previous study, we demonstrated the utility of LAESI-MS to explore the spatial distribution of metabolites in soybean nodules infected by WT *B. japonicum* (Stopka *et al.*, 2017). The metabolites detected and identified were similar to those identified through bulk MS analyses; however the LAESI-MS technique provided additional information on their spatial distribution. The absence of spatial variation in ion suppression effects in LAESI-MS of plant tissues has been demonstrated in the literature. Early demonstration of meaningful relative metabolite abundances in molecular imaging of plant tissues by LAESI-MS showed that the spatial variations of secondary metabolite levels agreed with the pigmentation pattern in variegated leaves (Nemes *et al.*, 2008). Ion suppression effects for relative and absolute quantitation for other matrixes and analytes by LAESI-MS have been considered in the literature. Successful relative quantitation of antibiotics in the presence of microbial metabolite gradients and an agar gel matrix was demonstrated (Li *et al.*, 2016). Absolute quantitation of a neurotoxin in over 180 shellfish samples by LAESI-MS was demonstrated against regulatory laboratory results and certified reference materials (Beach *et al.*, 2016).

As part of the technical validation of the method, we also demonstrated in-source fragmentation of only certain molecules, whereas another study reported no in-source fragmentation (Stopka *et al.*, 2017). To provide stronger confidence in our results, in a separate study, we utilized a different MS technique, MALDI-MSI, where we spatially mapped all metabolites (including those found via LAESI-MS) in a three-dimensional (3D) configuration within soybean nodules (Veličković *et al.*, 2018).

These previous studies gave us the impetus to utilize LAESI-MS in a more biologically focused study aiming to characterize the metabolism associated with soybean nodule function. For example, a vital aspect of a functioning symbiosis is the exchange of carbon and nitrogen compounds between the host and symbiont (Vance and Heichel, 1991; Udvardi and Poole, 2013). To understand the metabolism occurring within the soybean roots that were infected with WT *B. japonicum*, we sampled three distinct areas of the primary root anatomy (Figure S1a). Two areas were sampled at the uninfected and infected root areas,

which were located both on the primary root. The uninfected root area was approximately 2 cm away from the initial developing nodule and the infected root area was at the point-of-contact with the nodule. The third analyzed area was the intact nodules from the primary root (Figure S1a). By selectively targeting each of the distinctive areas, six biological root segments and nodules were analyzed using LAESI-MS. Within the uninfected root area, infected root area, and intact nodule, we detected approximately 112, 495, and 344 ions, known as spectral features, respectively, in the negative ion mode. These features are presumed to represent metabolic constituents, some of which were identified including 16, 37, and 49 metabolites within each respective root area (Table S1). To determine the area specific metabolites, multivariate statistical analysis was performed on the three sample groups. Using partial least squares discriminant analysis (PLS-DA), all three groups showed a high degree of separation (Figure S1b). Comparative analyses of infected and uninfected legumes was performed previously (Barsch *et al.*, 2006a; Brechenmacher *et al.*, 2010; Lardi *et al.*, 2016). However, these analyses were bulk measurements lacking any spatial information. In our experiments, we preserved the spatial information at the distant areas by selectively targeting the three different regions on the primary root segment infected by WT *B. japonicum*.

By sampling carbon and nitrogen metabolism in the different regions of the primary root, we were able to detect biomolecules that were highly abundant in particular sample groups (Figure S2 and Table S1). For example, soyasaponins, glucosides, and jasmonic acids (JAs) were detected in higher abundance in the infected root area (Figure S2a), whereas, in the uninfected root area, lipids, and sugars were mainly observed (Figure S2b). In the nodule sample group, several metabolites involved in biological nitrogen fixation were detected (e.g. adenine, glutamate, and glutamic acid) (Figure S2c). We were able to detect hormones, including gibberellin and JA, within the nodules only (Figure S2c).

Following an untargeted approach, pathway enrichment analysis was performed on each sample group using the Kyoto Encyclopedia of Genes and Genomes (KEGG) database (<https://www.genome.jp/kegg>) (Figure S3). In the infected root area, affected pathways included carbon metabolism and fatty acid biosynthesis (Figure S3a). As expected, the carbon metabolism pathway was elevated in the infected root area because this is the point of nodule attachment. In the uninfected root area (Figure S3b), we observed a higher fold enrichment of starch and sucrose metabolism, whereas amino sugar and nucleotide sugar metabolism were more abundant in the infected root area. Furthermore, nitrogen metabolism was strongly enriched within the nodule (Figure S3c), similar to the findings of Stopka *et al.* (2017). Altogether, LAESI-MS has the

capability to detect and localize specific metabolites at different regions of the whole, symbiotic nitrogen-fixing root.

Exploring the metabolite coverage of intact mutant nodules in soybean that are disrupted in symbiosis

Three nodule types were investigated, including the WT infected, *nifH*-infected, and the plant *sacpd-c* mutant. Recently, there has been renewed interest in the role that the plant immune system might play in nodule formation and maintenance (Cao *et al.*, 2017). To explore this within the context of nodule metabolism, we made use of *sacpd-c* mutant plants for which the nodules show altered ultrastructure and a concomitant increase in the expression of genes usually associated with a plant immune response (Gillman *et al.*, 2014; Krishnan *et al.*, 2016).

Nodules formed by the WT and *nifH* mutant strains could be easily differentiated by optical microscopy because of their distinct coloring of the infection zone. The WT infected nodules showed a reddish hue in the central region (as a result of the expression of leghemoglobin), whereas nodules infected by the *nifH* mutant strain

showed a white central zone (Figure 1a). These samples were analyzed using LAESI-MS in both positive and negative ion modes (Figure S4), in an effort to attain broad molecular coverage. Likewise, the *sacpd-c* nodules (Figure 1a) were also distinguishable by microscopy as a result of the central necrotic zone (Gillman *et al.*, 2014; Krishnan *et al.*, 2016). All three groups showed separation when looking at the PLS-DA plot in Figure 1(b). A closer examination using volcano plots provided the significantly abundant metabolites in each sample group compared to the WT infected nodules. These plots had customary cut-off values of 1 and -1 for $\log_2(\text{fold change})$ (FC) and $P < 0.05$ (Figures 1c,d). In total, 663 spectral features were detected in negative ion mode, of which 127 were significantly abundant in the *nifH* nodules and 113 were significantly abundant in the WT infected nodules (Figure 1c). When comparing the *sacpd-c* nodules and WT nodules, 683 spectral features were observed. Among these, 176 were more abundant in the *sacpd-c* nodules, whereas 66 were higher in the WT (Figure 1d). From these two volcano plots, some significantly regulated metabolites were annotated

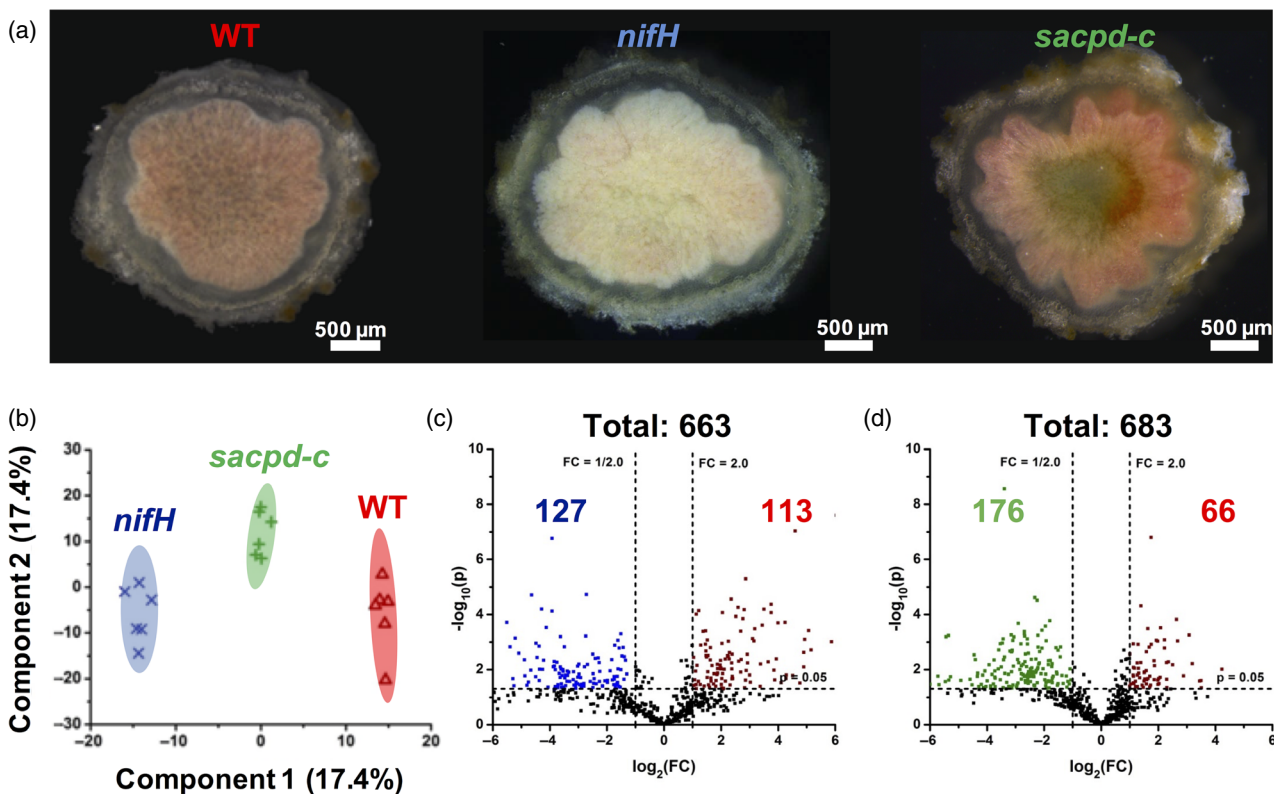


Figure 1. Metabolite profiling and compounds differentially present in wild-type (WT) and mutant nodules detected in negative ion mode.

(a) Brightfield images of 100-µm thick, nodule sections. Scale bars = 500 µm.

(b) Partial least squares discriminant analysis (PLS-DA) score plot showing the separation of sample types for the WT in red, *Bradyrhizobium japonicum nifH* mutant in blue, and *sacpd-c* mutant nodules in green.

(c, d) Volcano plots showing the number of spectral features biologically and statistically different (i.e. at least a fold change of 2 and a $P < 0.05$) between the various sample types. (c) Here, $FC = I_{nifH}/I_{WT}$; thus, compared to *B. japonicum* WT, significantly downregulated metabolites in *B. japonicum nifH* nodules are shown in blue and significantly upregulated species are shown in red. (d) Here, $FC = I_{sacpd-c}/I_{WT}$; thus, significantly downregulated metabolites in *B. japonicum sacpd-c* nodules are shown in green and significantly upregulated species are shown in red.

(Tables S2 and S3) and their roles were investigated in the symbiotic relationship.

Spatial profiling of *nifH* and WT nodule sections reveals differential metabolite distributions

A significant advantage of the *in situ* LAESI-MS technique is that it provides molecular information about metabolite abundance within the confines of the spatial areas sampled. For example, as part of our comparison of nodules infected by WT *B. japonicum* versus nodules infected by the *nifH* mutant strain, we used LAESI-MS to individually sample specific regions within the nodule (i.e. epidermis, cortex and central infection zone). Using a cryostat microtome, soybean root nodules were sectioned to 60 μm thickness and the mid-infrared laser probed the section to interrogate different anatomical regions of the sample. At each sample collection region, a mass spectrum in positive ion mode was obtained to allow ion tracking of metabolite intensities as a function of location based on absolute ion counts (Figure 2). Our previous work of single shot ablation in the inner and outer layer (Stopka *et al.*, 2017) showed that soyasaponin βg was localized in the nodule

epidermis and outer cortex, whereas heme *B*, reflecting leghemoglobin distribution, is a useful marker for the central infection zone.

Optical images before and after laser ablation of the WT and *nifH* nodules provided landmarks of the sampled areas (Figure 2a,b). The WT nodule lateral profiling consisted of six laser craters, two of which were at the outer cortex layer and four within the infection zone (Figure 2a). In this case, each crater was 300 μm in diameter. Using the metabolite markers, we tracked the distribution of soyasaponin βg and heme *B*. As observed before, only the outer layers revealed the presence of soyasaponin βg (Figure 2c), whereas the inner infection zone showed higher abundance of heme *B* (Figure 2e). Because the ablation shots resulted in a large crater, the sixth shot consisted of material from both the infection zone and the outer layer (Figure 2a). As a result of the smaller size of the *nifH* nodule, we could acquire only four ablation craters by LAESI-MS (Figure 2b). Similar to the WT nodules, soyasaponin βg was abundant at the first and fourth shot, which was localized at the outer layer (Figure 2d). However, consistent with the lack of red color, heme *B* showed lower

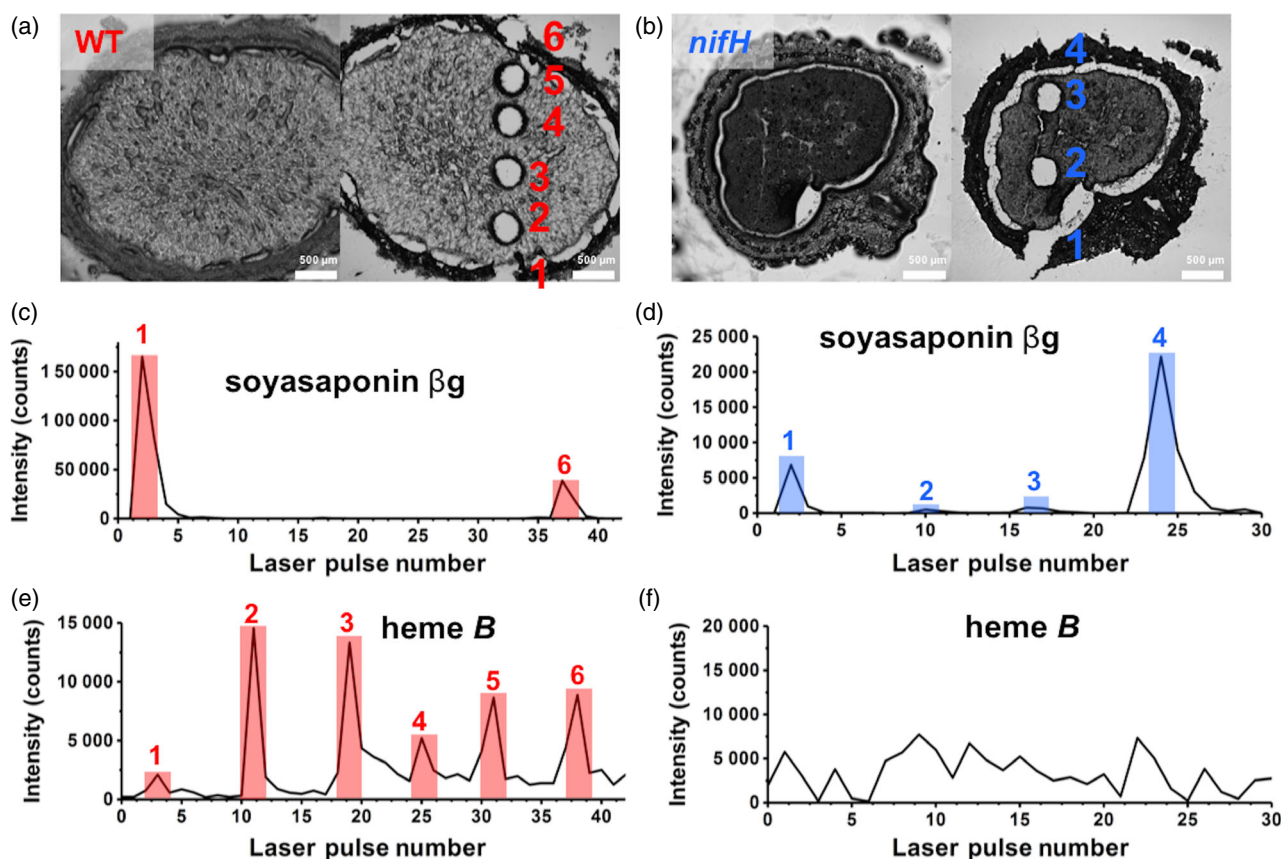


Figure 2. Spatial profiling of nodule sections inoculated with *Bradyrhizobium japonicum* wild-type (WT) or *nifH* mutant in positive ion mode. Bright field images of before and after ablation: (a) six ablation positions in WT nodule section, and (b) four ablation positions in nodule section with *nifH* mutant strain. Scale bars = 500 μm . Ion chromatograms (c and d) showing intensity profiles of soyasaponin βg at $m/z = 1069.56$ that is present in the outer layer of the nodules. Ion chromatograms for heme *B* at $m/z = 616.178$ that is present at higher intensities (e) in the WT nodule compared to the (f) *nifH* nodule.

abundance in the infection zone of the *nifH* nodule compared to the WT nodule (Figure 2f).

Using *in situ* LAESI-MS lateral profiling, we further explored the distribution of other metabolites at the different regions of the sectioned nodule. By way of example, Figure 3 shows the results of MS analysis in negative ion mode from the inner and outer regions of both the WT and *nifH* nodules after hierarchical clustering and multivariate statistical analysis. We detected species with a significant fold change > 2 and $P < 0.05$. In general from negative and positive ion modes, there were a total of 100 metabolites that were unique in the infection zone and 93 in the outer layer of the sectioned nodules that were infected by the WT *B. japonicum* or the *nifH* strain (Table S4). The outer layer and infection zone shared 44 common metabolites for both sectioned nodules. Taking a closer look at the outer layer, 56 distinctive metabolites were detected in the *nifH* sample and 81 in the WT sample. In the 'central zone',

110 metabolites were detected in the WT sample as compared to 34 in the *nifH* sample (Table S4). The column dendrogram that is displayed in the heat map showed separate nodes between the outer layer and the infection zone areas, as well as having a distinctive separation of metabolites (Figure 3a). Here, a clear distinction could be observed for the outer layer and infection zone of both sectioned nodules independent of bacterial strain. Using the PLS-DA model and combining the covariance and correlation loading profiles, S-plots were constructed (Figure 3b,c). The metabolites located at the wings of the S-plots are considered to be significant for each sample group. For example, in the S-plot of the WT and *nifH* nodules, the top wing represents metabolites significant in the outer layer and the bottom wing displays the infection zone (Figure 3b,c). Further inspection of these compounds was performed using box-and-whisker plots (Figure 3d) that were normalized by summing and Pareto scaling. For example,

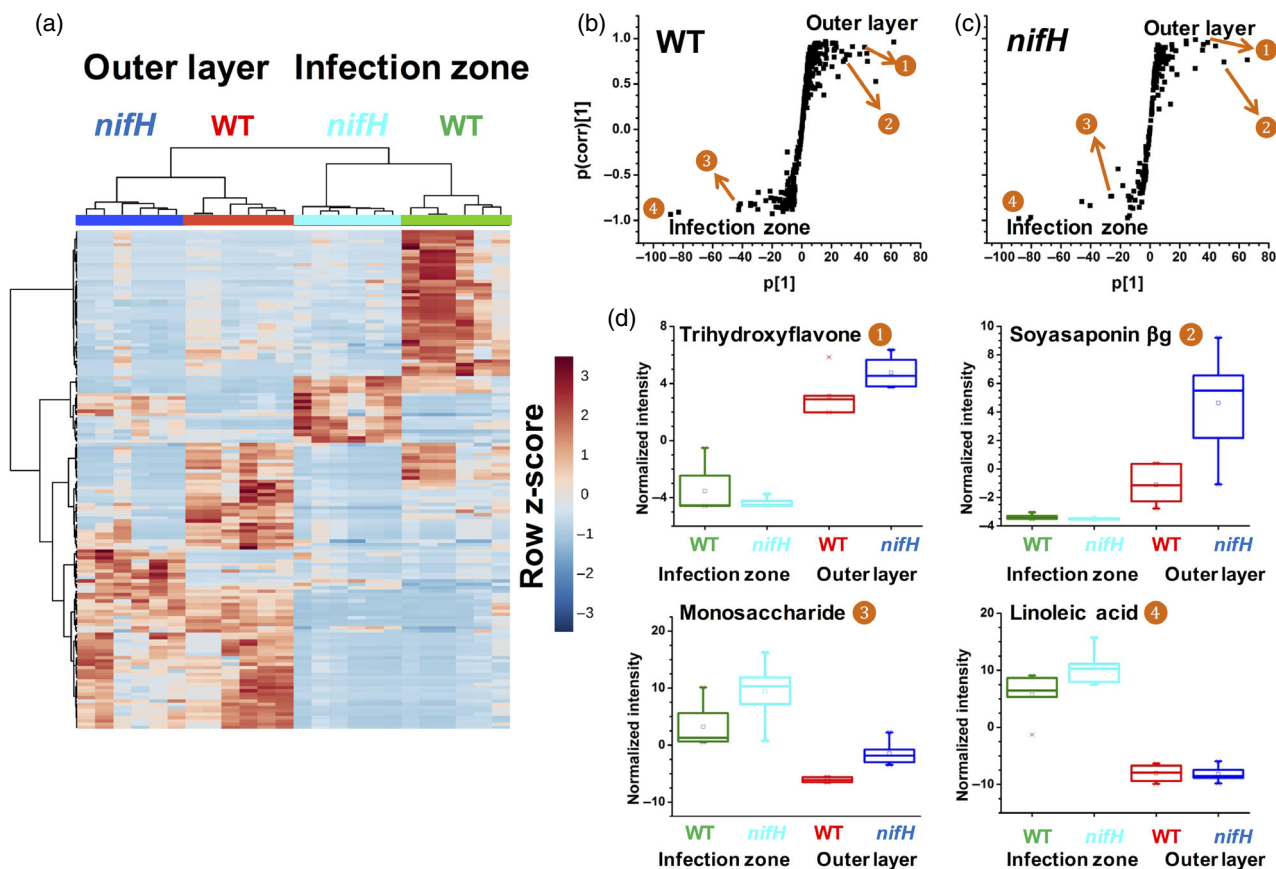


Figure 3. Comparison of metabolite abundance in outer layer and infection zone of wild-type (WT) and *nifH* nodule sections in negative ion mode.

(a) Heat map illustrating the relative abundance of metabolites in each sample, where each column represents a biological replicate ($n = 6$) from each sample type and each row corresponds to an m/z . Red shows greater relative abundance, whereas blue shows lower relative abundance.

S-plots represent correlation versus covariance for the metabolites in the inner and outer layers from (b) WT nodules and (c) *nifH* mutant nodules. Metabolites at the wings of the S-plots are specific to the infection zone (negative values) and the outer layer (positive values).

(d) Based on the S-plots, box-and-whisker plots were constructed to compare abundances for selected metabolites in the infection zone and outer layer of WT and *nifH* nodules.

The data were normalized, summing the spectral intensities for each sample and then the Pareto scaling was performed by using the square root of standard deviation as the scaling factor.

trihydroxyflavone and soyasaponin β g were more abundant in the outer layer than the infection zone of the WT and *nifH* nodules, whereas a monosaccharide and linoleic acid were highly localized in the infection zone. This analysis allowed us to determine what metabolites were preferentially present at the different layers of the nodule when comparing differently sampled nodules.

The metabolites that showed strong localization in either the outer or inner regions for both the WT versus *nifH* mutant nodules are listed in Table 1 from positive and negative ion mode datasets. In the infection zone of the WT nodules, metabolites such as glycerophospholipids [PA(16:0/18:1)], nucleobase-like molecules (adenine, cyclic-ADP ribose), gibberellin, and homoisocitrate were abundant, whereas, at the outer layer, tricarboxylic acids (homocitrate) and fatty acids (arachidic acid, tuberonic acid

glucoside) were higher in abundance. These are known metabolites from previous studies that have an essential role in the nitrogen-fixing symbiosis and organogenesis (Udvardi and Poole, 2013). Furthermore, metabolites involved in purine metabolism were highly abundant in the infection zone of the WT nodules (Table 1). In the *nifH* nodules, a lower abundance of purines was observed because this mutant displayed nitrogen-deficiency symptoms. Our results were similar to a study that used bulk metabolic analysis (Lardi *et al.*, 2016). However, in the present study, we were able to spatially localize these metabolites in the WT at the infection zone using LAESI-MS.

Additionally, jasmonate related metabolites (e.g. JA, methyl jasmonate, dihydrojasmonic acid, and hydroxyjasmonic acid) were abundant in the *nifH* mutant nodules within both the infection zone and outer layer (Table 1). JA

Table 1 Localization of metabolites that showed differential abundance detected in sections of nodules formed by either *Bradyrhizobium japonicum* wild-type (WT) or *nifH* mutant strain at the outer layer and the infection zone. These species had a significant fold change, $FC = I_{nifH}/I_{WT} \geq 2$, and $P < 0.05$ and were from positive and negative ion mode datasets

<i>nifH</i>			WT		
Compound	KEGG ID	Log ₂ (FC)	Compound	KEGG ID	Log ₂ (FC)
Infection zone					
Jasmonic acid ^{a,c,-,*}	C08491	-4.6	Choline ^{d,+,*}	C00114	3.9
Glycosyl glycerol-phosphate ^{a,c,-,**}	C01225	-4.3	Coniceine ^{e,+,**}	C10138	3.8
<i>N</i> -Feruloylglycine ^{e,-,**}		-3.3	Trihydroxy-tetramethoxyflavone glucoside ^{a,-,**}		3.6
Heptose ^{a,-,*}	C02076	-3.0	PA(16:0/18:1) ^{c,-,*}	C00416	3.1
Hydroxy dimethoxyflavone glucoside ^{d,-,*}		-3.0	Adenine ^{b,+,**}	C00147	3.0
Epoxyoctadecenoic acid ^{a,c,-,**}	C08368	-2.5	Acetyl-glutamic acid ^{a,c,-,**}	C03871	2.8
Oxoocatadecatrienoic acid ^{a,c,-,**}	C16320	-2.4	Gluconic acid ^{d,-,**}	C00257	2.5
Trihydroxyflavanone glucoside ^{d,-,*}	C09099	-2.1	Cyclic-ADP ribose ^{d,-,*}	C13050	2.5
Dihydrojasmonic acid ^{a,c,-,**}	C16309	-1.9	Coumesterol ^{a,c,-,**}	C10205	2.3
Methyl jasmonate ^{a,-,*}	C11512	-1.5	Hexose phosphate ^{a,c,-,**}	C01097	1.6
Outer layer					
Heptose ^{a,-,**}	C02076	-4.3	Trihydroxy-tetramethoxyflavone glucoside ^{a,-,**}		6.0
<i>N</i> -Feruloylglycine ^{e,-,**}		-4.2	Trihydroxyoctadecenoic acid ^{a,-,**}	C14833	3.0
Glycosyl glycerol-phosphate ^{a,c,-,**}	C01225	-4.2	Ajmaline ^{d,-,*}	C06542	2.5
Hydroxyjasmonic acid ^{a,-,**}	C21385	-3.3	Gibberellin ^{b,-,*}	C01699	2.2
Dissaccharide ^{a,c,+,**}	C00208	-2.5	Acetyl-glutamic acid ^{a,c,-,*}	C03871	2.1
Tetrahydroxyflavanone glucoside ^{a,c,-,*}	C16408	-2.0	Methylcitrate/homoisocitrate ^{a,-,*}	C01251	1.7
Vanillic acid ^{d,-,*}	C06672	-1.7	Arachidic acid ^{d,-,**}	C06425	1.2
Phosphocholine ^{d,+,*}	C00588	-1.6	Tuberonic acid glucoside ^{a,c,-,**}	C08558	1.1
Oxoocatadecatrienoic acid ^{a,c,-,**}	C16320	-1.2	Gluconic acid ^{a,c,-,**}	C00514	1.0

^aCompounds assigned based on ultra-high mass accuracy of 21T-Fourier transform ion cyclotron resonance-mass spectrometry (MS).

^bCompounds assigned based on in-house tandem MS of standards performed under identical conditions.

^cCompounds assigned based on tandem MS databases comparisons (<http://metlin.scripps.edu>; NIST/EPA/NIH Mass Spectral Library Version 2.2).

^dCompounds assigned from Stopka *et al.* (2017).

^eCompounds assigned from Veličković *et al.* (2018).

+Positive ion mode.

-Negative ion mode.

* $P < 0.05$.

** $P < 0.005$.

is a phytohormone that not only is essential for plant development, but also plays a role in the response to wounding and plant defense against biotic and abiotic stresses (Liechti and Farmer, 2002; Wasternack, 2007; Wasternack and Hause, 2013; Koo, 2018). However, JA biosynthesis is also upregulated at the transcriptional level during nitrogen deprivation (Pauwels *et al.*, 2009). Hence, elevation of JA within the *nifH* nodules may simply be a reflection of nitrogen deprivation, although we cannot exclude the possibility that the elevation of JA levels could also reflect induction of a plant immunity response.

The *sacpd-c* mutant nodules reveal dramatic nodule ultrastructure and metabolite distribution changes

Nodules formed on *sacpd-c* mutant (FN8) plant roots have morphological defects, such as the formation of central cavities or necrotic lesions, which were not observed in WT nodules (Figure 1a). The *sacpd-c* mutant bacteroid ultrastructure was distinctive, where the cells close to the necrotic lesion were in various stages of degradation (Gillman *et al.*, 2014). The presence of the central necrotic zone is a distinctive feature of the *sacpd-c* mutant nodules and therefore of particular interest. We sectioned at 60 μm thickness at the center of the whole nodule, where the necrotic lesion was visualized. The slices ($n = 6$) were used for the lateral profiling across the whole section and an example of a slice is shown in Figure S5(a). In total, there were eight ablation craters, and, for each crater, we obtained mass spectra including the outer layer at shot 1 and the lesion at shot 4 (Figure S5b). From the mass spectra, we were able to track the abundance of metabolites that were localized and distributed throughout the section of the nodule (Figure S5c). For example, adenosine was localized abundantly in the necrotic lesion at the third, fourth, and sixth shots. However, there was no abundance of adenosine at the fifth shot. Because the lesion area is thin and a fragile feature, limited material could be sampled (Figure S5a,c). Also, the fifth shot was at the starting point of the central necrotic zone as shown in the older nodule around 28 days (Figure S6b). Heme *B* was detected, which was more abundant in the infection zone compared to the necrotic lesion, whereas dihydroxyflavone was only localized in the outer layer. As a result of the large sampling area and fine structural features of the *sacpd-c* nodules, lateral profiling was limited in spatial resolution compared to the *nifH* and WT profiling. Several laser shots sampled material from both the different layers and necrotic regions; thus, to improve molecular distribution mapping in this case, a higher spatial resolution is required.

Thus, instead of lateral profiling, we used selective targeting of the infection zone of a WT nodule ($n = 10$) and the lesion of the *sacpd-c* nodule ($n = 10$) for comparison (Figure 4a,b). This allowed us to have a significant

statistical analysis with respect to capturing the metabolites that might be responsible for these necrotic regions and the significant compounds present in the healthy WT nodules in positive ion mode (Figure 4). The PLS-DA showed separation between the WT and the *sacpd-c* ablation craters (Figure 4c). In total, 89 significantly different spectral features were detected from this analysis. Fifteen features were significantly more abundant within the lesion area of the *sacpd-c* mutant nodules and 33 were significantly more abundant in the infection zone of the WT nodules (Figure 4d). The metabolites that were considered significant in each case were then ordered by their FC impact (Table 2). In general, the lesion of the *sacpd-c* was composed of sugars, saponins, organic acids (gluconic acid), and flavanone glucosides. By contrast, the infection zone of the WT contained metabolites related to biological nitrogen fixation, such as amino acids, nucleobase containing compounds, tricarboxylic acids, porphyrin and vitamins (heme *B*, riboflavin), and fatty acids. In addition, oleic acid was detected as well with a FC of 1.6 in the WT nodules relative to the *sacpd-c* nodules.

Fatty acids, including palmitic acid, stearic acid, oleic acid, linoleic acid, and linolenic acid, are known to be abundant in soybean plants (Lakhssassi *et al.*, 2017). Oleic acid content was found to be reduced in the *sacpd-c* mutants compared to WT soybean seeds. These results are consistent with our findings of significantly higher oleic acid content in the infection zone of the WT root nodules compared to *sacpd-c* lesions. In a previous study, we showed that the detected fatty acids are not breakdown products (Stopka *et al.*, 2017) (Figure S1). We analyzed the level of in-source fragmentation of lipids by examining standards for lipids detected in soybean samples with ESI and LAESI-MS. We found that using LAESI-MS 'in-source fragmentation of lipid species did not yield fatty acid ions, but rather the corresponding ketene cleavage products for the phosphatidylglycerol (PG) and phosphatidylcholine (PC) species' (Stopka *et al.*, 2017).

The class of compounds known as the triterpenoid saponins were found to be significantly more abundant in the necrotic lesion of the *sacpd-c* nodules with a FC ranging between 2 and 4 (Table 2). Saponins have surfactant properties that form stable soap-like foams (Hostettmann and Marston, 2005), which may explain the visual manifestation of water-soaked areas around the soft necrotic tissue within the nodules from the *sacpd-c* plants. External factors, including various biotic and abiotic stimuli with elicitation of methyl jasmonate, a signal component in plant defense responses, can produce saponins (Faizal and Geelen, 2013). Along with the high presence of saponins detected in the *sacpd-c* nodules, we also detected significant accumulation of methyl jasmonate (FC = 3.24) in these nodules (Table S1). However, there was no change in JA and 12-oxophytodienoic acid (OPDA) levels in the

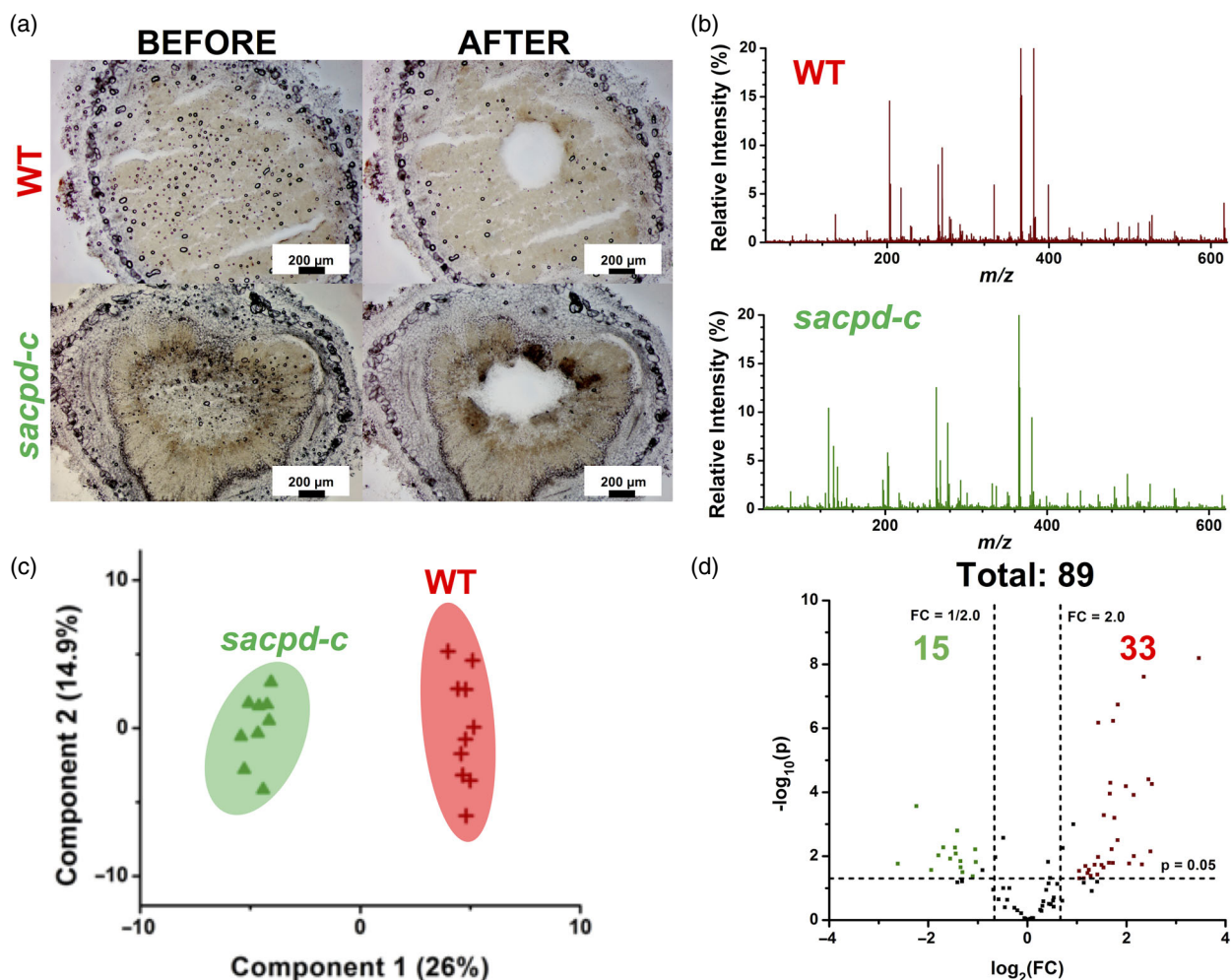


Figure 4. Comparison of ablation sampling craters and metabolite abundance in infection zone and necrotic lesion of wild-type (WT) and *sacpd-c* nodule sections in positive ion mode.

(a) Micrographs before and after ablation, where there is an ablation crater (diameter 300 μm) in the infection zone of the WT section, and an ablation crater (diameter 700 μm) in the lesion of the *sacpd-c* section. Scale bars = 200 μm.

(b) Average mass spectra from 50 to 620 m/z sampling areas of WT and *sacpd-c* nodules to show small molecule differences.

(c) Partial least squares discriminant analysis (PLS-DA) score plot showing the separation of sample types from the infection zone of the WT (red), and from the lesion of the *sacpd-c* mutant nodules (green).

(d) Volcano plot showing the number of metabolites from the selected m/z region that were statistically different (i.e. at least a fold change of 2 and a $P < 0.05$) between nodules, where $FC = I_{sacpd-c}/I_{WT}$, and significantly downregulated metabolites in *Bradyrhizobium japonicum sacpd-c* nodules compared to WT are shown in green and significantly upregulated species are shown in red.

sacpd-c mutant nodules. In Krishnan *et al.* (2016), the JA levels were reduced and OPDA levels were significantly higher by LC-tandem MS for bulk measurements of *sacpd-c* nodules. These levels can possibly be observed at the later stages of nodule development because their samples were observed at 30 days, whereas we observed them at 21 days in the present study. Moreover, it was shown that exogenous methyl jasmonate results in a suppression of nodulation (Nakagawa and Kawaguchi, 2006). However, there was no difference in the number of nodules between the WT and *sacpd-c* mutant lines at both 15 and 30 days (Krishnan *et al.*, 2016). Overall, we found that the *sacpd-c* mutant nodules stimulated the abundance of saponins.

These metabolites likely reflect the elevated plant defense response in the *sacpd-c* mutant nodules.

Metabolomic analysis of doubly infected soybean nodules does not support the presence of cell autonomous sanctions

A number of studies have posited the idea that the host plant can sanction ineffective or poorly fixing rhizobia to prevent the high occurrence of 'cheaters', comprising rhizobia that can infect but do not fix nitrogen (Singleton and Stockinger, 1983; Kiers *et al.*, 2003; Simms *et al.*, 2005; Sachs *et al.*, 2010; Oono *et al.*, 2011). Arguments have been made that sanctioning likely occurs at the level of the

Table 2 Top 16 molecular species that were identified in sections of soybean root nodules from either the infection zone of wild-type (WT) or from *sacpd-c* mutant plants at the necrotic lesion. These species had a significant fold change, $FC = I_{sacpd-c}/I_{WT} \geq 2$ and $P < 0.05$

<i>sacpd-c</i> (lesion)			WT (infection zone)		
Compound	KEGG ID	Log ₂ (FC)	Compound	KEGG ID	Log ₂ (FC)
Trihydroxyflavone ^{a,b,-,*}	C01477	-4.4	PA(16:0/18:1) ^{c,-,**}	C00416	6.7
Flavon malonyl glucoside ^{d,-,**}		-4.2	Reduced glutathione ^{d,+,**}	C00051	5.4
Soyasaponin I ^{a,b,-,**}	C08983	-3.8	PE(18:1/18:2) ^{c,-,*}	C00157	2.9
Heptose ^{a,-,**}	C02076	-3.6	Butene tricarboxylate ^{a,-,**}	C16579	2.1
Pentose ^{c,-,**}	C00181	-3.5	PE(16:0/18:1) ^{c,-,**}	C13877	2.0
Dehydrosoyasaponin I ^{a,c,-,**}	C13837	-3.0	Riboflavin ^{d,+,**}	C00255	1.9
Soyasaponin II ^{d,-,**}	C12081	-3.0	PG(16:0/18:1) ^{c,-,**}	C13883	1.8
Gluconic acid ^{a,c,-,*}	C00257	-3.0	S-Adenosylmethionine ^{d,e,+,**}	C00019	1.6
Tryptophan ^{a,c,-,*}	C00078	-3.0	Cyclohexylammonium ^{d,+,**}	C00571	1.6
Soyasaponin ag ^{d,-,*}	C08982	-3.0	Oleic acid ^{d,-,*}	C00712	1.6
Dihydroxyisoflavone ^{a,c,-,**}	C14344	-2.9	PI(16:0/18:2) ^{c,-,**}		1.5
Soyasaponin V ^{d,-,**}		-2.2	Jasmonoyl aminocyclopropane carboxylate ^{d,+,**}		1.5
Dihydroxy methoxyflavone glucoside ^{d,-,*}	C10381	-2.1	Methylcitrate/homoisocitrate ^{a,-,**}	C01251	1.5
Tetrahydroxyflavanone glucoside ^{a,c,-,**}	C16408	-2.0	UDP-hexose ^{e,-,*}	C00052	1.4
N-Feruloylglycine ^{e,-,*}		-1.8	Heme b ^{d,+,**}	C00032	1.3
Glucarate ^{a,-,*}	C00879	-1.4	PA(18:2/18:2) ^{c,-,**}		1.1

^aCompounds assigned based on ultra-high mass accuracy of 21T-Fourier transform ion cyclotron resonance-mass spectrometry (MS).

^bCompounds assigned based on in-house tandem MS of standards performed under identical conditions.

^cCompounds assigned based on tandem MS databases comparisons (<http://metlin.scripps.edu>; NIST/EPA/NIH Mass Spectral Library Version 2.2).

^dCompounds assigned from Stopka *et al.* (2017).

^eCompounds assigned from Veličković *et al.* (2018).

⁺Positive ion mode.

⁻Negative ion mode.

* $P < 0.05$.

** $P < 0.005$.

nodule in indeterminate nodulating plants, where the bacteroids are terminally differentiated and, hence, there is no advantage for the 'cheaters' with regard to subsequent growth. However, there remained the possibility that sanctioning could occur at the level of individual bacteroids of determinate nodulating plants, such as soybean, because some fraction of the bacteroids do retain the ability for limited cell division and, to some extent, can regrow from senescent nodules (Mergaert *et al.*, 2006). Indeed, recent studies (Regus *et al.*, 2015; Regus *et al.*, 2017) have examined this question using two determinate nodulating plant species, *Acmispon strigosus* and *Lotus japonicus*. Based on microscopy and histology, it was reported that sanctioning occurred at the level of the plant cell and was cell autonomous. That is, within doubly infected nodules, only those sectors infected by the fix^- rhizobia showed signs of early senescence, which they equated with sanctioning (Regus *et al.*, 2015; Regus *et al.*, 2017). The idea that sanctioning within nodules could be cell autonomous was suggested by Maunoury *et al.* (2010), based on the histology of *Medicago truncatula* indeterminate nodules.

Because most plant responses to stress are to some degree systemic, the idea of 'cell autonomous' sanctions within legume nodules seemed worthy of investigation,

especially given our ability to spatially analyzed metabolite distribution using LAESI-MS. Hence, we established doubly infected soybean nodules using the protocols of Regus *et al.* (2017) and analyzed the fix^- and fix^+ sectors separately. As indicated previously, the sampled sectors could be easily distinguished by their relative colors as visualized using a stereomicroscope (Figure S7a). Also, the WT rhizobia expressed green fluorescent protein (GFP) and, hence, we were able to visualize the different sectors using the fluorescence microscope (Figure S8). Note that, in nodules infected solely by the WT strain expressing GFP, there were no significant changes in morphology or metabolite distribution relative to those not expressing GFP.

Overall, eight biologically replicated nodules were analyzed from separate plants that were infected by a 3:7 (WT: *nifH* mutant) ratio. A sample of the analysis is shown in Figure 5(a) and Figure S7(b-c), which shows the two distinct sectors being sampled by the laser. The green outline represents the effective rhizobia (CI WT; CI stands for co-inoculated) sector that had a lighter contrast color, whereas the yellow outline shows the ineffective rhizobia (CI *nifH*) sector as a result of a darker contrast (Figure 5a). After the sectioned nodules were ablated at the two different sectors,

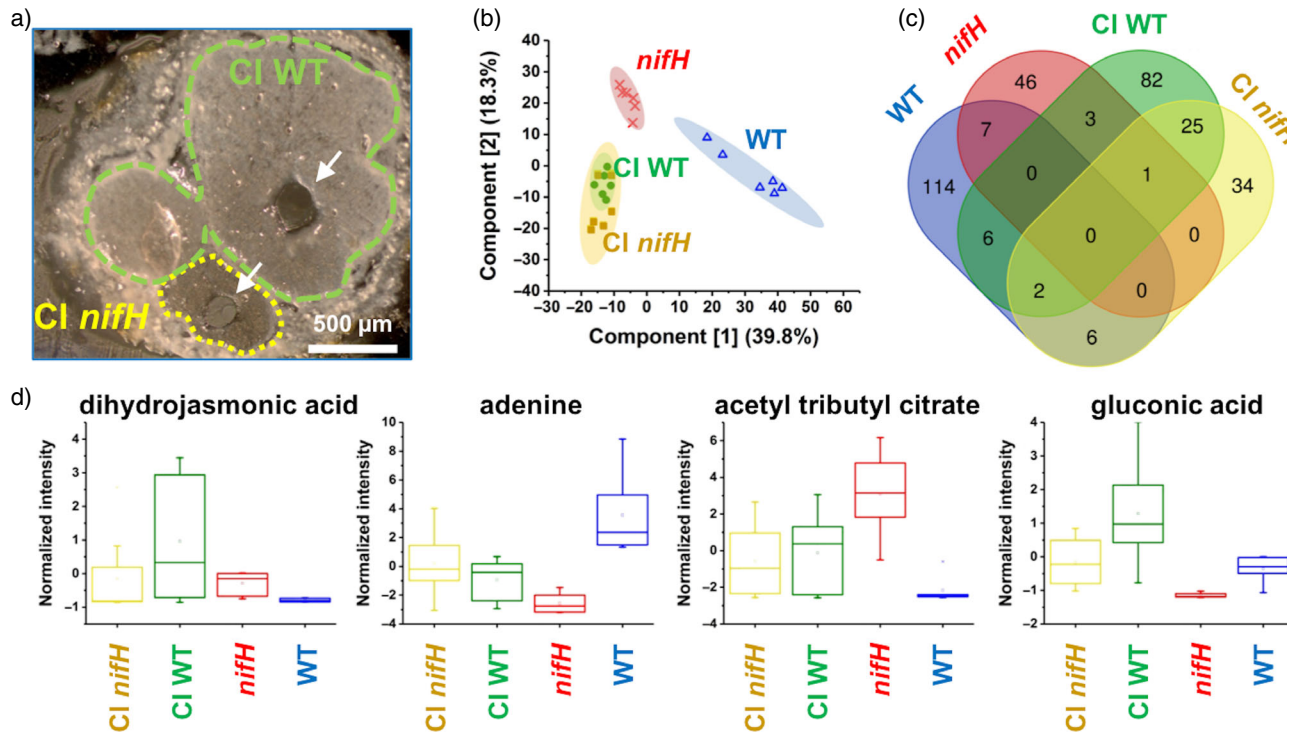


Figure 5. Metabolite abundance in sectors of nodules co-infected by *Bradyrhizobium japonicum* wild-type (WT) and *nifH* strains in negative ion mode. (a) Optical image of a co-infected soybean root nodule section that contained two sectors; a co-inoculated WT (CI WT) shown in green and a co-inoculated *nifH* mutant (CI *nifH*) shown in yellow. Each sector was targeted by laser ablation electrospray ionization-mass spectrometry for analysis with a spot size of approximately 200 μm in diameter. Arrows indicate the laser ablation craters. (b) The partial least squares discriminant analysis (PLS-DA) score plot of WT, *nifH* and co-inoculated sectors revealed separation; however, the two sectors in the co-inoculated nodules, CI WT and CI *nifH*, showed an overlap. (c) A Venn diagram showing the number of biologically and statistically significant metabolites that were detected in the four sampled regions. (d) Box-and-whisker plots for selected metabolites comparing normalized intensities. The data were normalized by summing and Pareto scaling.

the data were collected and analyzed statistically in a PLSDA score plot in negative ion mode (Figure 5b). The plot included the comparison between three sets of sampled nodules: (i) nodules that were infected by WT *B. japonicum* (presented in blue); (ii) nodules that were infected by the *nifH* mutant *B. japonicum* (red); and (iii) nodules that were 3:7 co-inoculated that have sectors of CI WT (green) and CI *nifH* (yellow). As expected, there was a separation between single infected WT and *nifH* nodules. However, the two co-inoculated samples (CI WT and CI *nifH*) showed significant overlap with each other and were not considered separated (Figure 5b). A 3D PLSDA plot that showed the three major components was used to explore the lack of separation among the co-inoculated samples (Figure S9). We were able to confirm the ultrastructural differences between the WT and fix^- sectors, as reported by Regus *et al.* (2017), whereas the metabolic data suggested that both sectors were likely under metabolic stress and could not be considered normal. Hence, although the data are consistent with the idea of sanctions acting at the level of individual nodules, they are inconsistent with the notion that the plant can sanction at the level of individual infected cells or sectors within a single nodule.

Approximately 200 spectral features were detected from each of the sectioned nodules in negative ion mode. In terms of significant metabolites, there was a total of 326 with a significant fold change of $\text{FC} \geq 2$ and $P < 0.05$ from all sampled nodules as shown in the Venn diagram (Figure 5c). Each set of sampled areas (ablation spots at the infection zone or the specific sectors) within the nodules (WT, *nifH*, CI WT, and CI *nifH*) have their unique metabolites ranging between 30 and 120. Interestingly, there were only seven metabolites overlapping between the WT and the *nifH*, whereas 25 overlapped among the co-inoculated sectors (Figure 5c). The few metabolites that overlapped between two or three sets of sampled areas within the sectioned nodules include dihydrojasmonic acid that was only present at the *nifH* and CI WT and not detected at the CI *nifH* and WT (Figure 5d). By contrast, adenine was detected in the WT and the co-inoculated sectors, although there was a significantly higher abundance of adenine in the WT compared to all other samples. Acetyl tributyl citrate was present in the *nifH* and both sectors, whereas gluconic acid was detected in the WT and CI WT/*nifH* sectors. However, gluconic acid was significantly more abundant in the CI WT (Figure 5d).

Some metabolites were identified that were unique for each sampled nodule area. Table 3 and Table S5 list the metabolites that were identified and detected in the co-inoculated sectors. Metabolites that were involved in carbon metabolism showed a higher abundance in the co-inoculated sectors (Table 3). For example, gluconic acid and pentose had an intensity fold change of $\log_2(I_{CI\ WT}/I_{WT})$ -1.54 and -3.23 , respectively, in the CI WT sector relative to the WT sampled nodule. In addition, glucosides such as tetrahydroxyflavone glucoside and pinosresinol glucoside, were highly abundant in the CI WT sector relative to the WT sampled nodule (Table S5). However, adenine and heme B were significantly lower within the co-inoculated nodule sectors than in the WT nodule, whereas, interestingly, allantoin, a major ureide involved in nitrogen transport from soybean nodules, was elevated in the co-inoculated nodules (Table 3). These findings suggest that bacteroids within both sectors of the co-inoculated nodules lacked optimal conditions for nitrogen fixation

and, hence, were not supporting robust nitrogen assimilation. In addition, metabolites that were involved in flavonoid biosynthesis were detected largely in the co-inoculated regions relative to WT nodules (Table 3).

Metabolic pathways involved in nitrogen fixation were revealed

Upon detection and characterization of highly abundant metabolites from the root nodules in negative and positive ion modes (Tables 1 and 2; Tables S2–S4), we collected their KEGG identification numbers for pathway enrichment analysis in METABOANALYST 4.0 (<https://www.metaboanalyst.ca>) against the *Glycine max* (soybean) library. Comparing between the WT and *nifH* nodules, 50 metabolites were used for the WT and 25 for the *nifH* nodules. Additionally, 16 metabolites were used for the *sacpd-c* and 22 for the WT nodules. We obtained pathways using an untargeted approach that contained a fold enrichment values between 0.5 as a minimum and 31 as the maximum (Figure 6).

Table 3 Identified metabolites in sections of root nodules infected by *Bradyrhizobium japonicum* wild-type (WT), *nifH* mutant strain, or both strains. The nodules that were co-inoculated with both strains showed two distinctive sectors: co-inoculated WT (CI WT) sector and co-inoculated *nifH* (CI *nifH*) sector. Species that had a significant fold change, $FC \geq 2$ and $P < 0.05$, are shown in bold based on mass spectrometry

Pathways	Compound	KEGG ID	Log ₂ (FC)					
			WT versus <i>nifH</i>	WT versus CI WT	WT versus CI <i>nifH</i>	<i>nifH</i> versus CI WT	<i>nifH</i> versus CI <i>nifH</i>	CI W versus CI <i>nifH</i>
Amino acid biosynthesis	Acetyl glutamic acid ^{d,+}	C00624	-5.15	-4.55**	-4.89**	-6.34**	-6.48**	-1.30**
	Aminooctanoic acid ^{d,+}	C00327	1.46	-2.47**	-2.63*	-4.26**	-4.11**	-0.55
	Succinylornithine ^{g,+}	C03415	-1.74	-4.48**	-4.13*	-1.78*	-1.58	0.31
Purine metabolism	Heme B ^{a,c,+}	C00032	3.61*	7.9512**	0.03	-2.93*	-1.93	1.39*
	Adenine ^{d,+}	C00147	3.16**	1.53**	3.82*	-1.79*	-2.48*	-0.57
	Allantoin ^{d,+}	C01551	0.25*	-3.49**	-2.91**	-5.28**	-4.63**	-0.05
Carbon metabolism	Adenosine ⁺	NA	-1.44	-1.88*	-1.91*	-3.67**	-3.45*	-0.44
	Gluconic acid ^{a,c,g,-}	C00257	2.48**	-1.54*	-0.74	-4.29**	-3.80**	1.21*
	Pentose ^{c,-}	C00216	1.45**	-3.23*	-3.1*	-3.37*	-3.26*	0.89
Flavonoid biosynthesis	Sucrose-phosphate ^{e,+}	C16688	5.31**	-1.99	-1.99	-3.78*	-1.99	0.42
	Isoflavonoid ^{g,+}	NA	-2.57**	-4.97**	-4.14**	1.20*	1.50**	0.36
	Hydroxy methoxyisoflavone ^{d,+}	NA	7.35*	-6.68**	-6.66	-8.47**	-7.73*	-0.09
	Pinosresinol glucoside ^{f,+}	NA	0.90	-1.53*	-1.53	-3.32**	-1.53	1.12*
	Tetrahydroxyflavone glucoside ^{d,+}	NA	4.22*	-1.32*	-1.32	-3.11**	-1.32	0.46

^aCompounds assigned based on ultra-high mass accuracy of 21 T-Fourier transform ion cyclotron resonance-mass spectrometry (MS).

^bCompounds assigned based on in-house tandem MS of standards performed under identical conditions.

^cCompounds assigned based on tandem MS databases comparisons (<http://metlin.scripps.edu>; NIST/EPA/NIH Mass Spectral Library Version 2.2).

^dCompounds assigned from Stopka *et al.* (2017).

^eCompounds assigned from Velicković *et al.* (2018).

^fCompounds assigned from Stopka *et al.* (2019).

^gCompounds from Laith *et al.* (2020).

⁺Positive ion mode.

⁻Negative ion mode.

* $P < 0.05$.

** $P < 0.005$.

There were many pathways that were affected in either of the WT, *nifH*, or *sacpd-c* nodules. Some top pathways that were influenced in the *nifH* mutant nodules were alpha-linolenic acid metabolism, flavonoid biosynthesis, and indole alkaloid biosynthesis (Figure 6a). By contrast, the pathways that had a higher fold enrichment in the WT infected nodules were zeatin (cytokinin) biosynthesis, ABC transporters, riboflavin metabolism, starch and sucrose metabolism, and purine metabolism (Figure 6a). From the *sacpd-c* enrichment analysis, the pathways more abundant were flavone and flavonol biosynthesis, indole alkaloid biosynthesis, and diterpenoid biosynthesis (Figure 6b). The pathways with a higher fold enrichment in the WT relative to the *sacpd-c* nodules are mostly known BNF pathways: zeatin biosynthesis, lysine biosynthesis, cysteine and methionine metabolism, and sulfur relay system (Figure 6b). Thus, taken together, mutagenizing the rhizobial *nifH* and the soybean *sacpd-c* impacted the association of symbiosis and nodule morphology. The plant can sense the occurrence of competent and incompetent rhizobia within the nodule, which resulted in changes in several metabolites and pathways.

DISCUSSION

Over the history of BNF research, mutant bacteria or plants have been an indispensable resource for studying gene function in nodulation (Halverson and Stacey, 1986; Sadowsky *et al.*, 1991; Sanjuan *et al.*, 1994; Sagan *et al.*, 1995; Loh *et al.*, 2001; Kawaguchi *et al.*, 2002; Hossain *et al.*, 2006; Sandal *et al.*, 2006; Kachroo *et al.*, 2008; Yamaya-Ito *et al.*, 2017). In the present study, we aimed to use such mutants to demonstrate the utility of LAESI-MS spatial profiling, as well as to address interesting questions related to nodule metabolism.

LAESI-MS: a unique tool for spatially detecting metabolites within the nodule

In the present study, we found that purine metabolism was highly abundant in the infection zone of the WT nodules while, a low abundance of purines was observed in the *nifH* nodules since this mutant displayed nitrogen-deficiency symptoms. This is expected because *de novo* purine biosynthesis is required for the formation of ureides, which are the primary molecules used for nitrogen transport from soybean nodules. This biosynthesis is involved in the conversion of amino acids and nucleotides to monophosphates, followed by oxidation to xanthine, and, lastly, to a final ureide product, such as allantoin (Smith and Atkins, 2002; Baral *et al.*, 2016).

Additionally, other pathways, including zeatin (cytokinin) biosynthesis, ABC transporters, riboflavin metabolism, and starch and sucrose metabolism, had a higher fold enrichment in the WT infected nodules than the *nifH* mutant nodules. As expected, these pathways are involved with BNF and organogenesis. Also, infected nodules require carbon and nitrogen flux between the endosymbionts and the

plant host (Atkins, 1987). Zeatin biosynthesis is an important pathway for plant growth and development in general, especially for the development of nodules (Atkins, 1987; Udvardi and Poole, 2013). Indeed, activation of cytokinin perception is now recognized as a key event in the initiation of nodule formation (Oldroyd and Downie, 2008). Leghemoglobin is an oxygen carrier that must be present for the continuation of nitrogen fixation in the central infected zone of the nodules (Brewin, 1991). The bacteroids require an adequate supply of oxygen for respiration and leghemoglobin ensures that oxygen is present when necessary. As expected, there was a low abundance of heme B in *nifH* nodules, reflected in the white/pale pink coloration in the infection zone. Studies have shown that early senescence of nodules, associated with fix^- nodules, is not only a result of nitrogen deficiency triggered by ineffective nitrogen fixation (Banba *et al.*, 2001; Kumagai *et al.*, 2007), but likely also involves the activation of plant defense responses (Suganuma *et al.*, 2003).

In the WT nodules, within the infection zone, homocitrate (FC = 1.70) was found to be significantly elevated relative to the *nifH* nodules. Homocitrate is a component of the iron-molybdenum cofactor in the nitrogenase complex (Hakoyama *et al.*, 2009), which could account for its abundance because, in this case, we cannot discern whether the metabolite is originating from the bacteroids or from the plant. Iron is also crucial for nitrogen fixation because it is one of the elements that is required in nitrogenase cofactors. Nodules have elevated levels of this element and, hence, homocitrate could also play a role in iron chelation and transport (Moreau *et al.*, 1995; LeVier *et al.*, 1996; Moreau *et al.*, 1998; Udvardi and Poole, 2013). One study found that FEN1 (fail in enlargement of infected cells) encodes homocitrate synthase that is specific to the nodule-infected cells. The *fen1* host mutants were similar in nodule formation to fix^- mutants and homocitrate was absent within the nodules (Hakoyama *et al.*, 2009). Accordingly, this suggests that the homocitrate detected in the present study is of plant origin.

Lack of biological nitrogen fixation induces metabolites related to plant defense

Rhizobial infection and nodule formation are accompanied by the need to synthesize a variety of new membranes (e.g. symbiosome membrane that surrounds the bacteroids). Indeed, it was estimated that the capacity for membrane biogenesis would need to be upregulated at least 35-fold to fulfill the need for nodule formation (Roth and Stacey, 1989). This estimation is consistent with the relative upregulation of glycerophospholipid/glycerolipid biosynthesis found in WT nodules relative to that found in the various mutant nodules.

In plants, fatty acids play critical signaling roles, specifically in responses to abiotic and biotic stresses. These

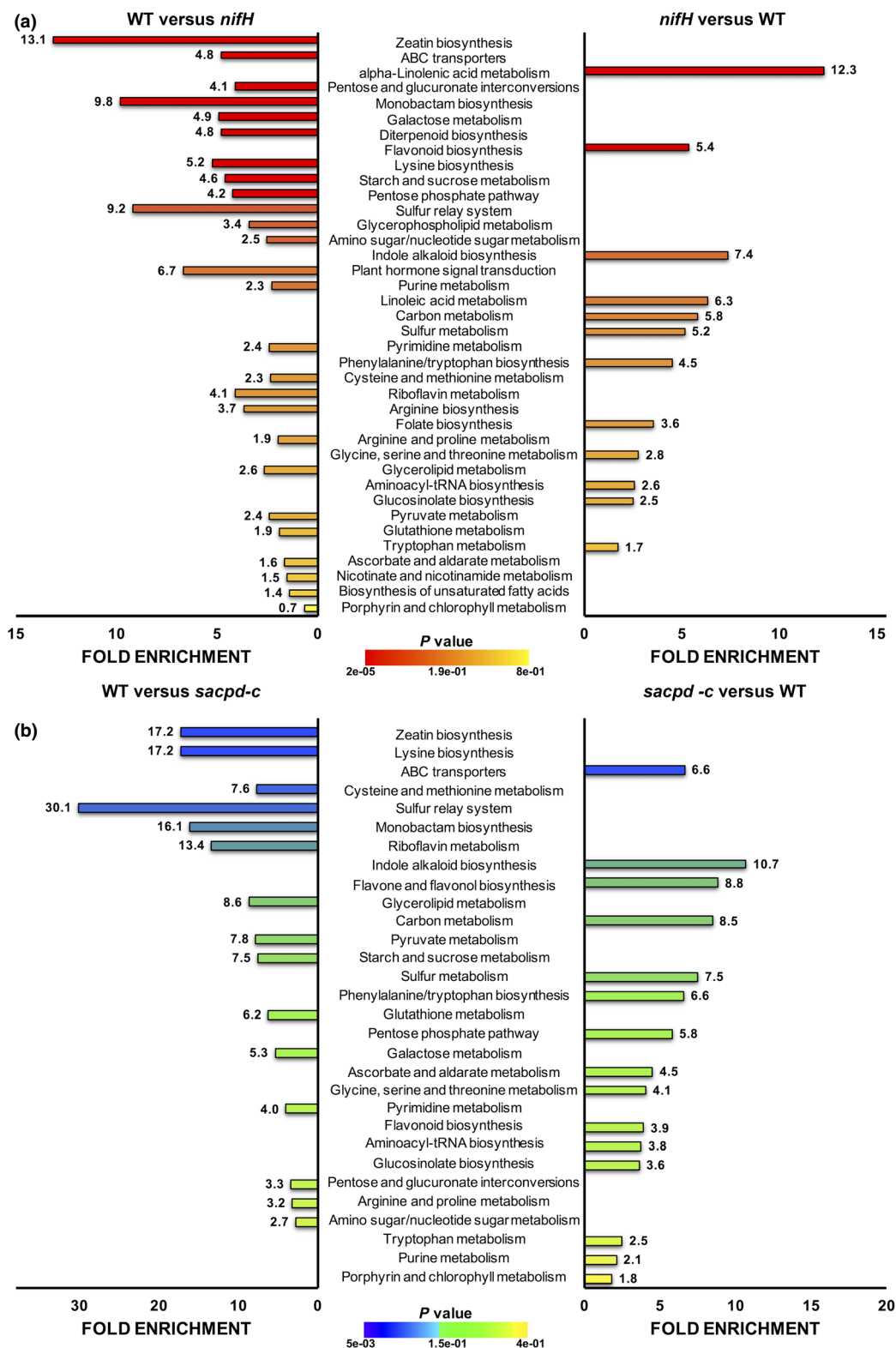


Figure 6. Pathway enrichment analysis comparing mutant and wild-type (WT) root nodules. Enriched pathways for (a) *nifH* and (b) *sacpd-c* versus WT and vice versa, which highlight up- and downregulated pathways related to biological nitrogen fixation and their statistical significance. Analysis was based on all identified metabolites with an ion intensity fold change ≥ 2 and a $P < 0.05$ using the METABOANALYST 4.0 web resource from both positive and negative ion mode datasets.

metabolites also function as energy storage molecules in all plant cells and are critical to membrane integrity and fluidity (Lim *et al.*, 2017). Of the fatty acids, linolenic acid is the most abundant in plant membranes and is required for nodulation because Brechenmacher *et al.* (2010) found an increase of linolenic and octadecenoic acids during the infection process. However, from our studies, we found that the linolenic acid metabolism was enriched by 12.3-fold in the *nifH* mutant relative to WT nodules (Figure 6a). Hakoyama *et al.* (2011) analyzed a *Lotus* symbiotic mutant, *sen1*, which forms nodules when infected by rhizobia, but does not fix nitrogen. This nodulation phenotype was similar to that in our study when we used mutagenized rhizobia (*nifH*) in soybean. Hakoyama *et al.* (2011) were able to identify the causal gene, *SEN1* (stationary endosymbiont nodule), which encodes an integral membrane protein and is essential for symbiosome and bacteroid differentiation in legume nodules. In our analyses, because the *nifH* nodules include an impairment of symbiosome integrity, we suggest that the host requires an abundance of linolenic acid related metabolites to support the membrane structure of the symbiosomes within the infection zone. Therefore, the increase of these fatty acids (linolenic and octadecenoic acids) is required for the upregulation of metabolic pathways for the synthesis and maintenance of infected-cell membranes during the infection process and nodulation.

However, although fatty acids are critical for membrane biogenesis, they also play a variety of roles in plant responses to abiotic and biotic stresses (Lim *et al.*, 2017). Polyunsaturated fatty acids (e.g. linolenic acid) are of particular importance and their accumulation correlates with increased pathogen resistance. For example, JA is derived from linolenic acid and is an example of oxygenated fatty acids, called oxylipins, many of which play important roles in plant defense. Previous studies have reported that disruption of the symbiosome membrane leads to the loss of BNF and the induction of endogenous defense-like responses in the host cell (Banba *et al.*, 2001; Kiers *et al.*, 2003; Oono *et al.*, 2011). Hence, the elevation in fatty acids (linolenic acid and octadecenoic acids) in *nifH* mutant nodules, relative to WT nodules, is of particular note and likely reflects the induction of defense pathways that have also been associated with the senescent morphology found in fix^- nodules. This is also consistent with the elevation of JA associated compounds in the *nifH* nodules, although we cannot rule out that the elevation of these compounds is also a response to nitrogen deprivation. Many studies applied JA exogenously to examine the initial perception and signaling events of the nitrogen-fixing symbiosis (Ding and Oldroyd, 2009; Hause and Schaarschmidt, 2009). JA application to legume roots affects the early epidermal responses during rhizobial infection. For example, JA acts as a negative regulator of many of the early signaling

events involved in nodule formation (Ding and Oldroyd, 2009). The addition of JA causes a decrease in nodule number on roots (Miwa *et al.*, 2006; Sun *et al.*, 2006). However, limited data are available regarding endogenous levels of JAs during the development of nodules. Zdyb *et al.* (2011) concluded that endogenous levels of JA are not involved in the development and function of root nodules in *Medicago*. There were no significant differences in JA between roots nodulated with WT *Sinorhizobium meliloti* or by mutant strains, unable to fix nitrogen, relative to non-nodulated roots. Transgenic *M. truncatula* with altered JA biosynthesis showed no alteration in nodule number and morphology (Zdyb *et al.*, 2011). These findings would suggest that, at least with regard to *M. truncatula*, endogenous JA has little involvement in nodulation. However, these conclusions may not extend to determinate nodulating plants such as soybean. In general, the metabolite data suggest that the plant can distinguish between nodules that are fixing adequate nitrogen and those that do not, resulting in changes in metabolism, some of which are consistent with the specific induction of processes normally associated with defense to plant pathogens.

Analysis of host sanctioning in doubly infected nodules

Histological and ultrastructural studies provide evidence that the plant can 'sanction' nodules providing inadequate nitrogen by limiting physiological inputs and reducing the survival of ineffective 'cheater' rhizobia (Singleton and Stockinger, 1983; Kiers *et al.*, 2003; Simms *et al.*, 2005; Sachs *et al.*, 2010; Oono *et al.*, 2011). Although the 'mechanisms' of this process remain unclear, the data strongly support the occurrence of such sanctioning at the level of the nodule. However, as noted above, previous studies, especially that of Regus *et al.* (2017), suggested that sanctioning, at least with regard to determinate nodulating plants, could occur at the level of specific bacteroids or at least within specific sectors of a single nodule. The studies that posit the occurrence of such 'cell autonomous' sanctioning have relied largely on microscopy and/or histology. Hence, we were interested in looking at this idea at a deeper level using the ability to spatially analyze metabolite distributions. LAESI-MS analysis was made possible by the very clear and obvious demarcation of the fix^- and fix^+ sectors based on microscopy, including fluorescent labeling of fix^+ sectors. This ability gave us confidence that cross contamination between the sectors sampled was minimal. The data obtained clearly indicate that, in doubly infected nodules, both the fix^- and fix^+ sectors were not physiologically normal. Overall, such doubly infected nodules, regardless of sector, showed symptoms of reduced nitrogen flux and suboptimal conditions for BNF (e.g. lower heme *B* levels). A variety of studies, as reviewed by Prell and Poole (2006), indicate that

carbon and nitrogen from both the host and bacteroids become mutually dependent, with each feeding back to modulate the metabolism of the other. This may provide the mechanism by which the plant sanctions specific nodules based on their overall nitrogen output. Hence, our data are inconsistent with the occurrence of cell autonomous sanctions, suggesting that the plant sanctions at the level of specific nodules likely through the action of feedback mechanisms that monitor carbon and nitrogen flux.

Although the combined results are consistent with this conclusion, an intriguing result was the finding that allantoin, the major ureide involved in nitrogen transport from soybean nodules, was elevated in the co-inoculated nodules [$\log_2(\text{FC}) = 3.49$] relative to nodules infected by WT *B. japonicum*. Fujihara and Yamaguchi (1980) reported that allantoin gradually increased over time in nodulated soybeans, reaching a maximum 60 days after sowing, under conditions where BNF was supported. Under their conditions, this correlated with the time of flowering, after which it is likely that carbon would primarily be directed to seed set and development. Consistent with this, at the late reproductive stage, the nitrogenase activity diminished, whereas there were still high concentrations of ureides in the senescent nodules. It was suggested that ureides formed at these late stages could arise from destruction of nucleic acids as a result of the plant's efforts to harvest nitrogen to support seed development (Fujihara and Yamaguchi, 1980). Hence, given the timing of our analysis at 21 days after sowing, ureide synthesis within the WT nodules would not be expected to occur at a high level. However, we assumed that the co-inoculated nodules were undergoing senescence because we detected an abundance of phenolic glucosides in the co-inoculated WT sector than the WT nodules. Previous studies have documented the accumulation of such phenolic compounds during nodule senescence (Veereshlingam *et al.*, 2004; Pislariu *et al.*, 2019). Therefore, assuming that the co-inoculated nodules were undergoing senescence, then they might be considered physiologically older and, thus, further along in their ability to produce ureides. Likewise, ureide production in these doubly infected, senescent nodules could also be relying on the degradation of nucleic acids as a source of nitrogen.

Metabolites involved in flavonoid biosynthesis had a higher abundance in the co-inoculated regions relative to WT nodules. Flavonoids are derived from the phenyl propanoid pathway and have a role in signaling and enhancing nodulation (Spaink *et al.*, 1987; Spaink *et al.*, 1991), whereas similar compounds from this pathway function as crucial molecules in the defense of plants against pathogens (Parniske *et al.*, 1990; Novák *et al.*, 2004). Indeed, one such compound, glyceollin, is known to increase in soybean nodules undergoing late season senescence (Karr *et al.*, 1992). It is

tempting to speculate that early senescence normally associated with fix^- nodules may be the result of the accumulation of bacterial toxic flavonoid-like compounds. For example, rhizobium mutants that were susceptible to specific phytoalexins showed reduced nodule occupancy when co-inoculated with the WT strain (Soedarjo and Borthakur, 1998).

Another function of flavonoid biosynthesis in symbiotic nitrogen-fixing nodules depends on the regulation of nitrogen availability. We found a metabolite profile consistent with reduced nitrogen flux within the co-inoculated nodules, whereas the data suggest that the carbon flux remains relatively high. The production of flavonoids in nodules is stimulated upon disruption of the carbon/nitrogen ratios (Hunter, 1983), which may be responsible in part for the elevation of flavonoids found in the co-inoculated nodules.

Alteration of fatty acid composition in the SAPCD-C mutant nodules resulted in dramatic changes in morphology and metabolism

SACPD-C plays a critical role in fatty acid biosynthesis, where the enzyme catalyzes the conversion of the saturated fatty acid, stearic acid, into the monounsaturated fatty acid, oleic acid (Shanklin and Cahoon, 1998; Kachroo *et al.*, 2007). Consistent with this, we found that oleic acid was more abundant in the WT nodules relative to the *sacpd-c* nodules. This finding is consistent with that reported by Gillman *et al.* (2014). Soybean *sacpd-c* mutants have been sought after because of the desire to increase stearate levels in seeds, which is useful for the production of specific margarines from soybean oil, as well as a reduction in adverse cardiovascular impacts (Hunter *et al.*, 2009; Gillman *et al.*, 2014). However, an unexpected and undesired effect of mutations in the *sacpd-c* gene is that they drastically affect nodule morphology. Interestingly, given their obvious differences in nodule appearance relative to the WT, the *sacpd-c* mutant nodules only showed an approximate 50% reduction in BNF, as measured by acetylene reduction (Gillman *et al.*, 2014; Krishnan *et al.*, 2016). However, this reduction might be sufficient to induce sanctioning mechanisms within the plant to reduce carbon flow to the nodule.

Krishnan *et al.* (2016) reported an elevation in the expression of specific genes normally associated with plant pathogen defense within the *sacpd-c* mutant nodules. For example, *Pathogenesis-Related 1* (PR-1) gene expression was significantly increased in 15- and 30-day nodules (Krishnan *et al.*, 2016). Our results are consistent with these findings because the mutant nodules also showed a significant elevation in alkaloid and flavonoid biosynthesis. Because the *sacpd-c* mutant plants develop nodules with a necrotic lesion at the central zone, flavonoid biosynthesis could reflect a general stress response and the production of antimicrobial compounds (Parniske *et al.*, 1990; Novák *et al.*, 2004). Furthermore, organic acids,

such as gluconic acid, accumulated in the necrotic lesion of the *sacpd-c* nodules with a $\log_2(\text{FC}) = 3.0$ (Table 2). Gluconic acid is an essential metabolite for rhizobacteria to solubilize minerals and insoluble phosphates, which increases phosphate availability for plants (Babu-Khan *et al.*, 1995). A previous study (de Werra *et al.*, 2009) noted a close association of gluconic acid metabolism with antagonistic activity against plant pathogens. There is no evidence that symbiosomes produce gluconic acid within the nodules. However, there is evidence that gluconic acid levels do affect the flux of phosphorus (Rosendahl *et al.*, 1991; Gaude *et al.*, 2004). The symbiosomes were apparently disintegrating within the necrotic area of the *sacpd-c* nodules, which would result in the release of free-living rhizobia that occupied the intercellular spaces, as observed by Krishnan *et al.* (2016). Perhaps, this effect may result in the release of bacterial elicitor compounds that would generally elevate plant defense signaling and metabolites associated with these processes.

It is unclear what role saponins and endogenous methyl jasmonate play within soybean nodules. Saponins can contribute to innate immunity as antimicrobial phytoprotectants in roots and root exudates (Faizal and Geelen, 2013; Tsuno *et al.*, 2017). For example, saponin is localized in the epidermal layer of root tips and lateral roots (Haralampidis *et al.*, 2002). Another study showed that saponins have a role in nodulation in *Medicago*, where they were localized at the meristematic and outer regions of the indeterminate nodules (Kemen *et al.*, 2014). Therefore, saponins may simply act as a chemical barrier in the outer root cell layers (e.g. epidermis). This correlates well with our results that show saponins localized at the outer layer of the WT, *nifH*, and *sacpd-c* nodules. However, it is noteworthy that saponins were abundant at the necrotic lesion of the *sacpd-c* mutant nodules, perhaps also playing an antimicrobial role. It was shown that saponins are activated when pathogenic fungi infect plant tissue and disrupt the membranes. As a result, saponins damage the fungal plasma membrane by forming membrane pores, which cause fungal cell death (Faizal and Geelen, 2013). Whether the synthesis of saponins is a result of or the cause of the necrosis found at the center of the *sacpd-c* mutant nodules cannot be determined at this time.

In the present study, our sampled mutant nodules (*nifH* and *sacpd-c*) showed metabolites that were involved in plant defense pathways. Therefore, our findings highlight the more recent recognition that plant innate immunity plays a crucial role in the legume symbiosis (Gourion *et al.*, 2015; Tóth and Stacey, 2015; Cao *et al.*, 2017). Metabolites such as linolenic acid, saponins, flavonoids, and JA were highly abundant either in the *nifH*, co-inoculated or *sacpd-c* nodules relative to the WT nodules. Hence, the present study provides metabolomic support for the notion that defects in BNF are associated with

induction of plant defense responses (Figure 7). More research is vital before we will be able to fully understand the role of plant innate immunity in nitrogen-fixing symbiosis.

We also sampled the three different regions of the primary root (uninfected root area, infected root area, and nodule area) that were infected by the wild-type bacteria. The distribution of metabolites in each area of the primary root correlated agreeably with the literature of carbon flux from the shoot to the nodule, which is responsible for nitrogen assimilation and bacterial respiration (Atkins, 1987; Sanchez *et al.*, 1991; Udvardi and Poole, 2013). Within the nodules, there was an abundance of hormones including gibberellin and JA, as expected, because these metabolites are involved in organogenesis and regulation of the mutualistic symbiosis (Ding and Oldroyd, 2009). Overall, these results align well with other BNF studies that showed the exchange of nitrogen and carbon resources between the host and the rhizobia (Udvardi and Poole, 2013).

The results of the present study contribute to a better understanding of the establishment of a functional symbiosis where metabolomic data is limited, especially with regard to the spatial distribution of metabolites within the nodule. Therefore, the observations of the present study demonstrate that LAESI-MS can be considered as a relatively high-throughput system for metabolically screening *in situ* tissues and mutants with respect to addressing a wide range of questions in plant biology. An exciting recent development is the ability of LAESI-MS to analyze the metabolome of single plant cells (Stopka *et al.*, 2018), which provides a means to investigate how single cell responses contribute individually to the overall plant response to rhizobial infection.

EXPERIMENTAL PROCEDURES

Plant growth and treatment

Soybean (*Glycine max* (L.) Merr.) seeds of 'Williams 82 and a fast neutron induced mutant line FN8 were used. The FN8 line was derived from cultivar 'Williams 82 and shown to contain a deletion in the gene encoding stearoyl-acyl carrier protein desaturase encoding gene C (*sacpd-c*) (Bolon *et al.*, 2011; Gillman *et al.*, 2014). Seeds were surface-sterilized with 20% (v/v) bleach for 10 min and rinsed five times in sterile water. The sterile seeds were planted into pots containing a mixture of sterilized vermiculite and perlite in a proportion of 3:1, respectively. At the time of sowing, the sterile seeds were inoculated with either *B. japonicum* USDA 110 (WT) or the *nifH* mutant (500 μl per seed). Bacterial growth is described in Methods S1. In the case of mixed inoculation (Methods S2), the WT and *nifH* mutant were mixed at ratios of 1:19 and 3:7, respectively, similar to those reported previously (Regus *et al.*, 2017). Plants were grown in the greenhouse under a 16:8 h light/dark photoperiod at 30°C. After 21 days of growth, the nodules attached to the primary root were harvested, immediately frozen in liquid nitrogen, and stored at -80°C until LAESI-MS analysis. Overall, the four nodule types analyzed were: (i) nodules

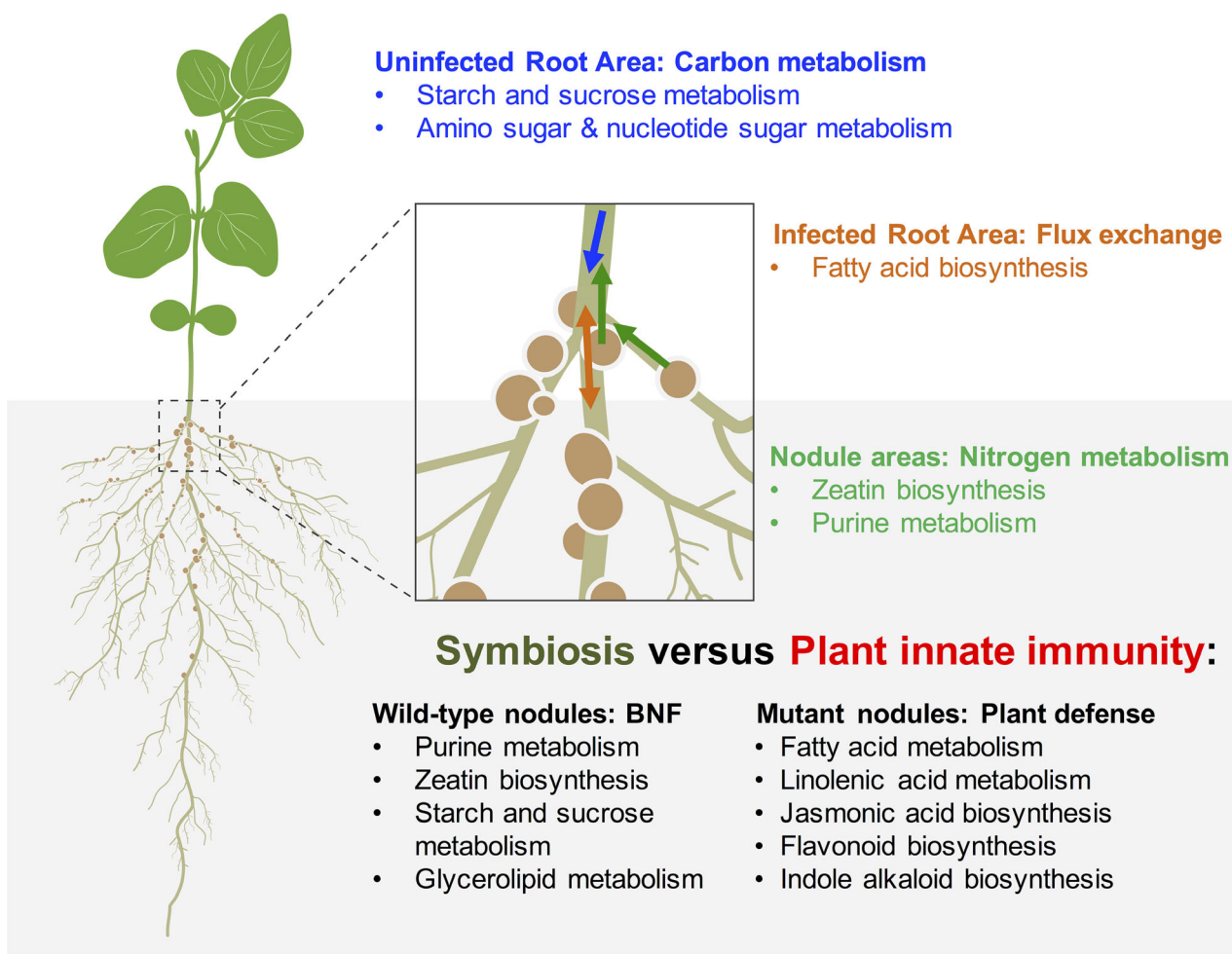


Figure 7. Co-evolution of metabolic pathways in the symbiotic partners between legumes and rhizobia.

A diagram of a whole soybean plant and a microscopic view of soybean root nodules integrated with this study's metabolomic findings, taken from both positive and negative ion mode datasets. The color font and arrow represent the location of specific pathways in the soybean root: (i) blue at the uninfected root area; (ii) orange at the infected root area; and (iii) green at the developing nodules resulted from Figures S1–S3. The metabolic pathways present in these three areas include: (i) carbon metabolism at the uninfected root area; (ii) flux exchange (fatty acid biosynthesis) at the infected root area; and (iii) nitrogen metabolism at the nodule. Different types of nodules [wild-type (WT) and mutant; *nifH* and *sacpd-c*] were analyzed and enriched pathways were curated from Figure 6. In general, the WT nodules were enriched in metabolic pathways involved in biological nitrogen fixation, whereas the mutant nodules displayed pathways related to plant defense.

infected by WT *B. japonicum*; (ii) nodules infected by the *nifH* mutant strain; (iii) nodules resulting from mix inoculation in a ratio of 3:7 WT:*nifH* mutant; and (iv) nodules formed by the WT bacterium on soybean *sacpd-c* mutant roots. For the phenotypic analysis, the nodules were sectioned at 100 μm using a vibratome and were imaged using a stereomicroscope (M205 FA; Leica, Buffalo Grove, IL, USA; <https://www.leica-microsystems.com>). The nodules with mixed infections were examined closely for phenotypic analysis, as described in Methods S2.

Metabolic profiling of free-living effective and ineffective rhizobia and soybean root nodules

All samples for LAESI-MS analysis, including *nifH*, *sacpd-c*, co-inoculated, and WT nodules, had a minimum of six biological replicates. For the analysis of *B. japonicum* WT and *B. japonicum nifH* mutant, cells were grown with antibiotics as indicated in Methods S2. The bacteria were sub-cultured and grown for 2 days

at 30°C in HM medium (Cole and Elkan, 1973) without antibiotics. When the bacterial culture reached an OD_{600} of 0.8 (10^8 cells ml^{-1}), the culture was centrifuged at 800 g for 10 min and washed three times with sterile water. The bacterial cell pellets were resuspended in 20 μl of deionized water. A 10- μl aliquot of the WT or *nifH* mutant culture was placed onto a microscope glass slide and analyzed directly by LAESI-MS.

For the whole nodule analysis, frozen samples were dipped into deionized water for 2 sec, blotted dry with a lint-free tissue, and placed on a microscope slide, positioning the root-distal region facing upward for LAESI-MS analysis. The samples were ablated in a raster formation using a laser energy of approximately 1.5 mJ per pulse with a repetition rate of 20 Hz. In this analysis, both the inner and outer layers of the nodules were sampled.

For lateral profiling, intact nodules were embedded in 2.5% carboxymethylcellulose in a mounting tray and placed in a cryostat microtome (CM1800; Leica Microsystems Inc., Nussloch,

Germany; <https://www.leica-microsystems.com>) that was set to -10°C for approximately 30 min until the samples were frozen in the embedding medium. The embedded nodules were affixed onto a specimen mount and sectioned to 60- μm thickness and thaw-mounted directly onto a microscope slide. The sectioned nodule samples were imaged using a microscope (IX71; Olympus, Tokyo, Japan; <https://www.olympus-lifescience.com>) before and after LAESI-MS analysis to determine the interrogated sample areas. In addition, Methods S2 describes how the co-inoculated nodules were observed before LAESI-MS analysis. Using a manual stage, the sections were laterally profiled by ablating each sample area with three laser shots of approximately 1.5 mJ per pulse. Between two to six ablated spots were obtained from each lateral section. LAESI-MS instrumentation (Stopka *et al.*, 2017), pathway analysis, and metabolite identification are described in Methods S3–S7.

ACKNOWLEDGEMENTS

The material is based on work supported by the US Department of Energy (DOE), Office of Biological and Environmental Research (OBER) under award number DOE-FOA-0001192 and National Science Foundation (NSF) Plant Genome Program under award number IOS-1734145. We thank Dr Hans-Martin Fischer from the Eidgenössische Technische Hochschule Zürich, CH-8093 Zürich, Switzerland, for providing us the *B. japonicum* fix⁻ mutant H1 (*nifH*) strain. We thank Frank Baker and Alexander Jurkevich from the Molecular Cytology Core at the C. S. Bond Life Sciences Center, the University of Missouri, for their help on the microscope images. We acknowledge Yaya Cui, Cuong Xuan Nguyen, Marina Cotta, Tomas Pellizzaro Pereira, Fernanda Plucani do Amaral, and Thalita Tuleski for helping to grow numerous soybean plants. We also thank Md Shakhawat Hossain, as well as Katalin Tóth, Marina Cotta, Arati Poudel, Ritesh Kumar, and Fernanda Plucani do Amaral, for reading and editing earlier versions of this manuscript. J. Robil is acknowledged for the graphic design of Figure 7. B.J.A. would like to acknowledge the University of Missouri's College of Agriculture, Food and Natural Resources (CAFNR) and Office of Graduate Studies for the George Washington Carver Fellowship and Gus T. Ridgel Fellowship; and the DOE Mickey Leland Fellowship. S.E. was supported by the University of Missouri's FRIPS (Freshmen research in plant Sciences) program.

AUTHOR CONTRIBUTIONS

BJA, SAS, CRA, AV, and GS designed the experiments. MGS provided the *sacpd-c* seeds. BJA, SAS, SE, and LS performed the research. BJA, SAS, SE, LS, YL, and DX analyzed the data. BJA wrote the article with input from SAS, CRA, MGS, DX, DWK, LP, LS, AV, and GS.

CONFLICT OF INTERESTS

The authors declare no conflict of interest.

DATA AVAILABILITY STATEMENT

Raw metabolomic data are available upon request to the corresponding author.

SUPPORTING INFORMATION

Additional Supporting Information may be found in the online version of this article.

Figure S1. Metabolite profiling of soybean root anatomy when infected by WT *B. japonicum* using LAESI-MS in negative ion mode.

Figure S2. Box-and-whisker plots of significant metabolites that were highly abundant in the different areas of the primary root from negative ion mode.

Figure S3. Fold enrichments represented by bar lengths for pathways highly affected in soybean primary roots by WT *B. japonicum* infection.

Figure S4. Mass spectra from LAESI-MS.

Figure S5. Comparison of metabolite profiles for 60- μm nodule sections derived from *sacpd-c* mutant plants in positive ion mode.

Figure S6. Microscopy images of nodule ultrastructure from mutant plant line *sacpd-c*.

Figure S7. Phenotypic screening of co-inoculated nodules at different rhizobia inoculum ratios.

Figure S8. Fluorescence microscope images of *nifH* and 3:7 (WT: *nifH*) co-inoculated nodules.

Figure S9. 3D PLS-DA score plot contrasting LAESI-MS data of WT, *nifH*, and co-inoculated nodules.

Table S1. List of identified and unknown peaks that were highly abundant in the different areas of the WT primary root based on Figures S1–S3.

Table S2. List of metabolites relating to Figure 1 with significant fold changes in the *sacpd-c* and *nifH* compared to the WT with a FC, of ≥ 2 and $P < 0.05$.

Table S3. List of identified and unknown compounds relating to Figure 1 in negative and positive ion mode datasets.

Table S4. List of compounds relating to Figure 3 with significant fold changes in the infection zone and outer layer when comparing nodules formed by either *B. japonicum* WT or *nifH* mutant strain.

Table S5. Annotated metabolites that were significantly different between nodule types.

Methods S1. Bacterial growth conditions.

Methods S2. Nodules that were infected by mix-inoculums

Methods S3. Instrumentation for LAESI-MS.

Methods S4. Data and pathway analysis.

Methods S5. Sample preparation for tandem electrospray ionization mass spectrometry (ESI-MS/MS).

Methods S6. Tandem electrospray ionization mass spectrometry (ESI-MS/MS).

Methods S7. Metabolite identification.

REFERENCES

- Atkins, C. (1987) Metabolism and translocation of fixed nitrogen in the nodulated legume. *Plant Soil*, **100**, 157–169.
- Babu-Khan, S., Yeo, T.C., Martin, W.L., Duron, M.R., Rogers, R.D. and Goldstein, A.H. (1995) Cloning of a mineral phosphate-solubilizing gene from *Pseudomonas cepacia*. *Appl. Environ. Microbiol.* **61**, 972–978.
- Banba, M., Siddique, A.-B.-M., Kouchi, H., Izui, K. and Hata, S. (2001) *Lotus japonicus* forms early senescent root nodules with *Rhizobium etli*. *Mol. Plant-Microbe Interact.* **14**, 173–180.
- Baral, B., da Silva, J.A.T. and Izaguirre-Mayoral, M.L. (2016) Early signaling, synthesis, transport and metabolism of ureides. *J. Plant Physiol.* **193**, 97–109.
- Barsch, A., Carvalho, H.G., Cullimore, J.V. and Niehaus, K. (2006a) GC-MS based metabolite profiling implies three interdependent ways of ammonium assimilation in *Medicago truncatula* root nodules. *J. Biotechnol.* **127**, 79–83.
- Barsch, A., Tellström, V., Patschkowski, T., Küster, H. and Niehaus, K. (2006b) Metabolite profiles of nodulated alfalfa plants indicate that

- distinct stages of nodule organogenesis are accompanied by global physiological adaptations. *Mol. Plant-Microbe Interact.* **19**, 998–1013.
- Beach, D.G., Walsh, C.M., Cantrell, P., Rourke, W., O'Brien, S., Reeves, K. and McCarron, P. (2016) Laser ablation electrospray ionization high-resolution mass spectrometry for regulatory screening of domoic acid in shellfish. *Rapid Commun. Mass Spectrom.* **30**, 2379–2387.
- Beatty, P.H. and Good, A.G. (2011) Future prospects for cereals that fix nitrogen. *Science*, **333**, 416–417.
- Bolon, Y.T., Haun, W.J., Xu, W.W. et al. (2011) Phenotypic and genomic analyses of a fast neutron mutant population resource in soybean. *Plant Physiol.* **156**, 240–253.
- Brechenmacher, L., Lei, Z., Libault, M., Findley, S., Sugawara, M., Sadowsky, M.J., Sumner, L.W. and Stacey, G. (2010) Soybean metabolites regulated in root hairs in response to the symbiotic bacterium *Bradyrhizobium japonicum*. *Plant Physiol.* **153**, 1808–1822.
- Brewin, N.J. (1991) Development of the legume root nodule. *Annu. Rev. Cell Biol.* **7**, 191–226.
- Cao, Y., Halane, M.K., Gassmann, W. and Stacey, G. (2017) The role of plant innate immunity in the legume-rhizobium symbiosis. *Annu. Rev. Plant Biol.* **68**, 535–561.
- Charpentier, M. and Oldroyd, G. (2010) How close are we to nitrogen-fixing cereals? *Curr. Opin. Plant Biol.* **13**, 556–564.
- Cole, M.A. and Elkan, G.H. (1973) Transmissible resistance to penicillin G, neomycin, and chloramphenicol in *Rhizobium japonicum*. *Antimicrob. Agents Chemother.* **4**, 248–253.
- Colebatch, G., Desbrosses, G., Ott, T., Krusell, L., Montanari, O., Kloska, S., Kopka, J. and Udvardi, M.K. (2004) Global changes in transcription orchestrate metabolic differentiation during symbiotic nitrogen fixation in *Lotus japonicus*. *Plant J.* **39**, 487–512.
- de Werra, P., Péchy-Tarr, M., Keel, C. and Maurhofer, M. (2009) Role of gluconic acid production in the regulation of biocontrol traits of *Pseudomonas fluorescens* CHA0. *Appl. Environ. Microbiol.* **75**, 4162–4174.
- Denison, R.F. (2000) Legume sanctions and the evolution of symbiotic cooperation by rhizobia. *Am. Nat.* **156**, 567–576.
- Desbrosses, G.G., Kopka, J. and Udvardi, M.K. (2005) *Lotus japonicus* metabolic profiling. Development of gas chromatography-mass spectrometry resources for the study of plant-microbe interactions. *Plant Physiol.* **137**, 1302–1318.
- Ding, Y. and Oldroyd, G.E. (2009) Positioning the nodule, the hormone dicum. *Plant Signal. Behav.* **4**, 89–93.
- Faizal, A. and Geelen, D. (2013) Saponins and their role in biological processes in plants. *Phytochem. Rev.* **12**, 877–893.
- Fujihara, S. and Yamaguchi, M. (1980) Nitrogen fixation and allantoin formation in soybean plants. *Agric. Biol. Chem.* **44**, 2569–2573.
- Gaude, N., Tippmann, H., Flegmetakis, E., Katinakis, P., Udvardi, M. and Dörmann, P. (2004) The galactolipid digalactosyldiacylglycerol accumulates in the peribacteroid membrane of nitrogen-fixing nodules of soybean and *Lotus*. *J. Biol. Chem.* **279**, 34624–34630.
- Gemperline, E., Jayaraman, D., Maeda, J., Ané, J.-M. and Li, L. (2015) Multifaceted investigation of metabolites during nitrogen fixation in *Medicago* via high resolution MALDI-MS imaging and ESI-MS. *J. Am. Soc. Mass Spectrom.* **26**, 149–158.
- Gillman, J.D., Stacey, M.G., Cui, Y.Y., Berg, H.R. and Stacey, G. (2014) Deletions of the SACPD-C locus elevate seed stearic acid levels but also result in fatty acid and morphological alterations in nitrogen fixing nodules. *BMC Plant Biol.* **14**, 143.
- Gourion, B., Berrabah, F., Ratet, P. and Stacey, G. (2015) Rhizobium-legume symbioses: the crucial role of plant immunity. *Trends Plant Sci.* **20**, 186–194.
- Hahn, M., Meyer, L., Studer, D., Regensburger, B. and Hennecke, H. (1984) Insertion and deletion mutations within the nif region of rhizobium-japonicum. *Plant Mol. Biol.* **3**, 159–168.
- Hakoyama, T., Niimi, K., Watanabe, H., Tabata, R., Matsubara, J., Sato, S., Nakamura, Y., Tabata, S., Jichun, L. and Matsumoto, T. (2009) Host plant genome overcomes the lack of a bacterial gene for symbiotic nitrogen fixation. *Nature*, **462**, 514–517.
- Hakoyama, T., Niimi, K., Yamamoto, T., Isobe, S., Sato, S., Nakamura, Y., Tabata, S., Kumagai, H., Umehara, Y. and Brossuleit, K. (2011) The integral membrane protein SEN1 is required for symbiotic nitrogen fixation in *Lotus japonicus* nodules. *Plant Cell Physiol.* **53**, 225–236.
- Halverson, L.J. and Stacey, G. (1986) Effect of lectin on nodulation by wild-type *Bradyrhizobium japonicum* and a nodulation-defective mutant. *Appl. Environ. Microbiol.* **51**, 753–760.
- Harada, K. and Fukusaki, E. (2009) Profiling of primary metabolite by means of capillary electrophoresis-mass spectrometry and its application for plant science. *Plant Biotechnol.* **26**, 47–52.
- Haralampidis, K., Trojanowska, M. and Osbourn, A.E. (2002) Biosynthesis of triterpenoid saponins in plants. In *History and Trends in Bioprocessing and Biotransformation* (Dutta, N.N., Hammar, F., Haralampidis, K., et al. eds). Vol. 75, Berlin, Heidelberg: Springer, pp. 31–49.
- Hardy, R. and Havelka, U. (1975) Nitrogen fixation research: a key to world food? *Science*, **188**, 633–643.
- Hause, B. and Schaarschmidt, S. (2009) The role of jasmonates in mutualistic symbioses between plants and soil-born microorganisms. *Phytochemistry*, **70**, 1589–1599.
- Hossain, M.S., Umehara, Y. and Kouchi, H. (2006) A novel Fix symbiotic mutant of *Lotus japonicus*, Ljsym105, shows impaired development and premature deterioration of nodule infected cells and symbiosomes. *Mol. Plant-Microbe Interact.* **19**, 780–788.
- Hostettmann, K. and Marston, A. (2005) *Saponins*. Cambridge: Cambridge University Press.
- Hunter, J.E., Zhang, J. and Kris-Etherton, P.M. (2009) Cardiovascular disease risk of dietary stearic acid compared with trans, other saturated, and unsaturated fatty acids: a systematic review. *Am. J. Clin. Nutr.* **91**, 46–63.
- Hunter, W.J. (1983) Soybean root and nodule nitrate reductase. *Physiol. Plant.* **59**, 471–475.
- Kachroo, A., Fu, D.-Q., Havens, W., Navarre, D., Kachroo, P. and Ghabrial, S.A. (2008) An oleic acid-mediated pathway induces constitutive defense signaling and enhanced resistance to multiple pathogens in soybean. *Mol. Plant-Microbe Interact.* **21**, 564–575.
- Kachroo, A., Shanklin, J., Whittle, E., Lapchuk, L., Hildebrand, D. and Kachroo, P. (2007) The Arabidopsis stearoyl-acyl carrier protein-desaturase family and the contribution of leaf isoforms to oleic acid synthesis. *Plant Mol. Biol.* **63**, 257–271.
- Karr, D., Emerich, D. and Karr, A. (1992) Accumulation of the phytoalexin, glyceollin, in root nodules of soybean formed by effective and ineffective strains of *Bradyrhizobium japonicum*. *J. Chem. Ecol.* **18**, 997–1008.
- Kawaguchi, M., Imaizumi-Anraku, H., Koiwa, H., Niwa, S., Ikuta, A., Syono, K. and Akao, S. (2002) Root, root hair, and symbiotic mutants of the model legume *Lotus japonicus*. *Mol. Plant-Microbe Interact.* **15**, 17–26.
- Kemen, A.C., Honkanen, S., Melton, R.E., Findlay, K.C., Mugford, S.T., Hayaishi, K., Haralampidis, K., Rosser, S.J. and Osbourn, A. (2014) Investigation of triterpene synthesis and regulation in oats reveals a role for β -amyryn in determining root epidermal cell patterning. *Proc. Natl Acad. Sci. USA*, **111**, 8679–8684.
- Kiers, E.T., Rousseau, R.A., West, S.A. and Denison, R.F. (2003) Host sanctions and the legume-rhizobium mutualism. *Nature*, **425**, 78–81.
- Koo, A.J. (2018) Metabolism of the plant hormone jasmonate: a sentinel for tissue damage and master regulator of stress response. *Phytochem. Rev.* **17**, 51–80.
- Krishnan, H.B., Alaswad, A.A., Oehle, N.W. and Gillman, J.D. (2016) Deletion of the SACPD-C locus alters the symbiotic relationship between *Bradyrhizobium japonicum* USDA110 and soybean, resulting in elicitation of plant defense response and nodulation defects. *Mol. Plant-Microbe Interact.* **29**, 862–877.
- Kumagai, H., Hakoyama, T., Umehara, Y., Sato, S., Kaneko, T., Tabata, S. and Kouchi, H. (2007) A novel ankyrin-repeat membrane protein, IGN1, is required for persistence of nitrogen-fixing symbiosis in root nodules of *Lotus japonicus*. *Plant Physiol.* **143**, 1293–1305.
- Laith, A.Z., Rikkita, K., Tina, T.H. et al. (2020) Single-cell metabolic profiling: metabolite formulas from isotopic fine structures in heterogeneous plant cell populations. *Anal. Chem.* **92**(10), 7289–7298. <https://doi.org/10.1021/acs.analchem.0c00936>
- Lakhssassi, N., Colantonio, V., Flowers, N.D., Zhou, Z., Henry, J., Liu, S. and Meksem, K. (2017) Stearoyl-acyl carrier protein desaturase mutations uncover an impact of stearic acid in leaf and nodule structure. *Plant Physiol.* **174**, 1531–1543.
- Lardi, M., Murset, V., Fischer, H.-M., Mesa, S., Ahrens, C.H., Zamboni, N. and Pessi, G. (2016) Metabolomic profiling of *Bradyrhizobium*

- diazoefficiens*-induced root nodules reveals both host plant-specific and developmental signatures. *Int. J. Mol. Sci.* **17**, 815.
- Larrainzar, E., Wienkoop, S., Weckwerth, W., Ladrera, R., Arrese-Igor, C. and González, E.M. (2007) *Medicago truncatula* root nodule proteome analysis reveals differential plant and bacteroid responses to drought stress. *Plant Physiol.* **144**, 1495–1507.
- LeVier, K., Day, D.A. and Gueriot, M.L. (1996) Iron uptake by symbiosomes from soybean root nodules. *Plant Physiol.* **111**, 893–900.
- Li, H., Balan, P. and Vertes, A. (2016) Molecular imaging of growth, metabolism, and antibiotic inhibition in bacterial colonies by laser ablation electrospray ionization mass spectrometry. *Angew. Chem. Int. Ed.* **55**, 15035–15039.
- Libault, M. (2018) Transcriptional reprogramming of legume genomes: perspective and challenges associated with single-cell and single cell-type approaches during nodule development. *Front. Plant Sci.* **9**, 1600.
- Liechti, R. and Farmer, E.E. (2002) The jasmonate pathway. *Science*, **296**, 1649–1650.
- Lim, G.-H., Singhal, R., Kachroo, A. and Kachroo, P. (2017) Fatty acid– and lipid-mediated signaling in plant defense. *Annu. Rev. Phytopathol.* **55**, 505–536.
- Loh, J.T., Yuen-Tsai, J.P.Y., Stacey, M.G., Lohar, D., Welborn, A. and Stacey, G. (2001) Population density-dependent regulation of the *Bradyrhizobium japonicum* nodulation genes. *Mol. Microbiol.* **42**, 37–46.
- Maunoury, N., Redondo-Nieto, M., Bourcy, M., Van de Velde, W., Alunni, B., Laporte, P., Durand, P., Agier, N., Marisa, L. and Vaubert, D. (2010) Differentiation of symbiotic cells and endosymbionts in *Medicago truncatula* nodulation are coupled to two transcriptome-switches. *PLoS ONE*, **5**, e9519.
- Mergaert, P., Uchiumi, T., Alunni, B., Evanno, G., Cheron, A., Catrice, O., Mausset, A.-E., Barloy-Hubler, F., Galibert, F. and Kondorosi, A. (2006) Eukaryotic control on bacterial cell cycle and differentiation in the Rhizobium–legume symbiosis. *Proc. Natl Acad. Sci. USA*, **103**, 5230–5235.
- Miwa, H., Sun, J., Oldroyd, G.E. and Allan Downie, J. (2006) Analysis of calcium spiking using aameleon calcium sensor reveals that nodulation gene expression is regulated by calcium spike number and the developmental status of the cell. *Plant J.* **48**, 883–894.
- Moreau, S., Day, D.A. and Puppo, A. (1998) Ferrous iron is transported across the peribacteroid membrane of soybean nodules. *Planta*, **207**, 83–87.
- Moreau, S., Meyer, J.-M. and Puppo, A. (1995) Uptake of iron by symbiosomes and bacteroids from soybean nodules. *FEBS Lett.* **361**, 225–228.
- Nakagawa, T. and Kawaguchi, M. (2006) Shoot-applied MeJA suppresses root nodulation in *Lotus japonicus*. *Plant Cell Physiol.* **47**, 176–180.
- Nemes, P., Barton, A.A., Li, Y. and Vertes, A. (2008) Ambient molecular imaging and depth profiling of live tissue by infrared laser ablation electrospray ionization mass spectrometry. *Anal. Chem.* **80**, 4575–4582.
- Nemes, P. and Vertes, A. (2007) Laser ablation electrospray ionization for atmospheric pressure, in vivo, and imaging mass spectrometry. *Anal. Chem.* **79**, 8098–8106.
- Novák, K., Lisá, L. and Škrádeľ, V. (2004) Rhizobial nod gene-inducing activity in pea nodulation mutants: dissociation of nodulation and flavonoid response. *Physiol. Plant.* **120**, 546–555.
- Oldroyd, G.E. (2013) Speak, friend, and enter: signalling systems that promote beneficial symbiotic associations in plants. *Nat. Rev. Microbiol.* **11**, 252–263.
- Oldroyd, G.E. and Downie, J.A. (2008) Coordinating nodule morphogenesis with rhizobial infection in legumes. *Annu. Rev. Plant Biol.* **59**, 519–546.
- Oono, R., Anderson, C.G. and Denison, R.F. (2011) Failure to fix nitrogen by non-reproductive symbiotic rhizobia triggers host sanctions that reduce fitness of their reproductive clonemates. *Proc. Roy. Soc. Lond. B Biol. Sci.* **278**, 2698–2703.
- Parniske, M., Zimmermann, C., Cregan, P. and Werner, D. (1990) Hypersensitive reaction of nodule cells in the glycine sp./*Bradyrhizobium japonicum*-symbiosis occurs at the genotype-specific level. *Botanica Acta*, **103**, 143–148.
- Pauwels, L., Inzé, D. and Goossens, A. (2009) Jasmonate-inducible gene: what does it mean? *Trends Plant Sci.* **14**, 87–91.
- Pislaru, C.I., Sinharoy, S., Torres-Jerez, I., Nakashima, J., Blancaflor, E.B. and Udvardi, M.K. (2019) The nodule-specific PLAT domain protein NPD1 is required for nitrogen-fixing symbiosis. *Plant Physiol.* **180**, 1480–1497.
- Prell, J. and Poole, P. (2006) Metabolic changes of rhizobia in legume nodules. *Trends Microbiol.* **14**, 161–168.
- Regus, J., Gano, K., Hollowell, A., Sofish, V. and Sachs, J. (2015) Lotus hosts delimit the mutualism–parasitism continuum of *B. radyrhizobium*. *J. Evol. Biol.* **28**, 447–456.
- Regus, J.U., Quides, K.W., O'Neill, M.R., Suzuki, R., Savory, E.A., Chang, J.H. and Sachs, J.L. (2017) Cell autonomous sanctions in legumes target ineffective rhizobia in nodules with mixed infections. *Am. J. Bot.* **104**, 1299–1312.
- Rosendahl, L., Glenn, A.R. and Dilworth, M.J. (1991) Organic and inorganic inputs into legume root nodule nitrogen fixation. In *Biology and biochemistry of nitrogen fixation* (Dilworth, M.J., and Glenn, A.R., eds). London: Elsevier London, pp. 259–291.
- Roth, L. and Stacey, G. (1989) Bacterium release into host cells of nitrogen-fixing soybean nodules: the symbiosome membrane comes from three sources. *Eur. J. Cell Biol.* **49**, 13–23.
- Sachs, J., Russell, J., Lü, Y., Black, K., Lopez, G. and Patil, A. (2010) Host control over infection and proliferation of a cheater symbiont. *J. Evol. Biol.* **23**, 1919–1927.
- Sadowsky, M.J., Cregan, P.B., Gottfert, M., Sharma, A., Gerhold, D., Rodriguez-Quinones, F., Keyser, H.H., Hennecke, H. and Stacey, G. (1991) The *Bradyrhizobium japonicum* nolA gene and its involvement in the genotype-specific nodulation of soybeans. *Proc. Natl Acad. Sci. USA*, **88**, 637–641.
- Sagan, M., Morandi, D., Tarengi, E. and Duc, G. (1995) Selection of nodulation and mycorrhizal mutants in the model plant *Medicago truncatula* (Gaertn.) after γ -ray mutagenesis. *Plant Sci.* **111**, 63–71.
- Sanchez, F., Padilla, J.E., Perez, H. and Lara, M. (1991) Control of nodulin genes in root-nodule development and metabolism. *Annu. Rev. Plant Biol.* **42**, 507–528.
- Sandal, N., Petersen, T.R., Murray, J., Umehara, Y., Karas, B., Yano, K., Kumagai, H., Yoshikawa, M., Saito, K. and Hayashi, M. (2006) Genetics of symbiosis in *Lotus japonicus*: recombinant inbred lines, comparative genetic maps, and map position of 35 symbiotic loci. *Mol. Plant-Microbe Interact.* **19**, 80–91.
- Sanjuan, J., Grob, P., Goettfert, M., Hennecke, H. and Stacey, G. (1994) NodW is essential for full expression of the common nodulation genes in *Bradyrhizobium japonicum*. *Mol. Plant Microbe Interact.* **7**, 364–369.
- Sato, T., Yashima, H., Ohtake, N., Sueyoshi, K., Akao, S., Harper, J.E. and Ohya, T. (1998) Determination of leghemoglobin components and xylem sap composition by capillary electrophoresis in hypernodulation soybean mutants cultivated in the field. *Soil Sci. Plant Nutr.* **44**, 635–645.
- Shanklin, J. and Cahoon, E.B. (1998) Desaturation and related modifications of fatty acids. *Annu. Rev. Plant Biol.* **49**, 611–641.
- Simms, E.L., Taylor, D.L., Povich, J., Shefferson, R.P., Sachs, J., Urbina, M. and Tausczik, Y. (2005) An empirical test of partner choice mechanisms in a wild legume–rhizobium interaction. *Proc. Roy. Soc. B Biol. Sci.* **273**, 77–81.
- Singleton, P. and Stockinger, K. (1983) Compensation against ineffective nodulation in soybean 1. *Crop Sci.* **23**, 69–72.
- Smith, P.M. and Atkins, C.A. (2002) Purine biosynthesis. Big in cell division, even bigger in nitrogen assimilation. *Plant Physiol.* **128**, 793–802.
- Soedarjo, M. and Borthakur, D. (1998) Mimosine, a toxin produced by the tree-legume *Leucaena* provides a nodulation competition advantage to mimosine-degrading *Rhizobium* strains. *Soil Biol. Biochem.* **30**, 1605–1613.
- Soga, T., Ohashi, Y., Ueno, Y., Naraoka, H., Tomita, M. and Nishioka, T. (2003) Quantitative metabolome analysis using capillary electrophoresis mass spectrometry. *J. Proteome Res.* **2**, 488–494.
- Spaink, H.P., Sheeley, D.M., van Brussel, A.A., Glushka, J., York, W.S., Tak, T., Geiger, O., Kennedy, E.P., Reinhold, V.N. and Lugtenberg, B.J. (1991) A novel highly unsaturated fatty acid moiety of lipo-oligosaccharide signals determines host specificity of *Rhizobium*. *Nature*, **354**, 125.
- Spaink, H.P., Wijffelman, C.A., Pees, E., Okker, R.J. and Lugtenberg, B. (1987) *Rhizobium* nodulation gene nodD as a determinant of host specificity. *Nature*, **328**, 337.
- Stacey, G. (2007) The *Rhizobium*-legume nitrogen-fixing symbiosis. In *Biology of the Nitrogen Cycle* (Bothe, H., Ferguson, S.J., and Newton, W.E., eds). London: Elsevier, p. 147–163.
- Stacey, G., Libault, M., Brechenmacher, L., Wan, J. and May, G.D. (2006) Genetics and functional genomics of legume nodulation. *Curr. Opin. Plant Biol.* **9**, 110–121.

- Stopka, S.A., Agtuca, B.J., Koppelaar, D.W., Paša-Tolić, L., Stacey, G., Vertes, A. and Anderton, C.R. (2017) Laser ablation electrospray ionization mass spectrometry with ion mobility separation reveals metabolites in the symbiotic interactions of soybean roots and rhizobia. *Plant J.* **91**, 340–354.
- Stopka, S.A., Khattar, R., Agtuca, B.J., Anderton, C.R., Paša-Tolić, L., Stacey, G. and Vertes, A. (2018) Metabolic noise and distinct subpopulations observed by single cell LAESI mass spectrometry of plant cells in situ. *Front. Plant Sci.* **9**, 1646.
- Stopka, S.A., Samarah, L.Z., Shaw, J.B. et al. (2019) Ambient metabolic profiling and imaging of biological samples with ultrahigh molecular resolution using laser ablation electrospray ionization 21 Tesla FTICR mass spectrometry. *Anal. Chem.* **91**(8), 5028–5035. <https://doi.org/10.1021/acs.analchem.8b05084>
- Suganuma, N., Nakamura, Y., Yamamoto, M., Ohta, T., Koiwa, H., Akao, S. and Kawaguchi, M. (2003) The *Lotus japonicus* Sen1 gene controls rhizobial differentiation into nitrogen-fixing bacteroids in nodules. *Mol. Genet. Genomics*, **269**, 312–320.
- Sun, J., Cardoza, V., Mitchell, D.M., Bright, L., Oldroyd, G. and Harris, J.M. (2006) Crosstalk between jasmonic acid, ethylene and Nod factor signaling allows integration of diverse inputs for regulation of nodulation. *Plant J.* **46**, 961–970.
- Tóth, K. and Stacey, G. (2015) Does plant immunity play a critical role during initiation of the legume-rhizobium symbiosis? *Front. Plant Sci.* **6**, 401.
- Tsuno, Y., Fujimatsu, T., Endo, K., Sugiyama, A. and Yazaki, K. (2017) Soyasaponins, a new class of root exudates in soybean (*Glycine max*). *Plant Cell Physiol.* **59**, 366–375.
- Udvardi, M. and Poole, P.S. (2013) Transport and metabolism in legume-rhizobia symbioses. *Annu. Rev. Plant Biol.* **64**, 781–805.
- Vance, C. and Heichel, G. (1991) Carbon in N₂ fixation: limitation or ex-site adaptation. *Annu. Rev. Plant Biol.* **42**, 373–390.
- Veereshlingam, H., Haynes, J.G., Penmetza, R.V., Cook, D.R., Sherrier, D.J. and Dickstein, R. (2004) nip, a symbiotic *Medicago truncatula* mutant that forms root nodules with aberrant infection threads and plant defense-like response. *Plant Physiol.* **136**, 3692–3702.
- Velicković, D., Agtuca, B.J., Stopka, S.A., Vertes, A., Koppelaar, D.W., Paša-Tolić, L., Stacey, G. and Anderton, C.R. (2018) Observed metabolic asymmetry within soybean root nodules reflects unexpected complexity in rhizobacteria-legume metabolite exchange. *ISME J.* **12**, 2335–2338.
- Vicente, E.J. and Dean, D.R. (2017) Keeping the nitrogen-fixation dream alive. *Proc. Natl Acad. Sci. USA*, **114**, 3009–3011.
- Wang, J.Y., Si, Z.Y., Li, F., Xiong, X.B., Lei, L., Xie, F.L., Chen, D.S., Li, Y.X. and Li, Y.G. (2015) A purple acid phosphatase plays a role in nodule formation and nitrogen fixation in *Astragalus sinicus*. *Plant Mol. Biol.* **88**, 515–529.
- Wasternack, C. (2007) Jasmonates: an update on biosynthesis, signal transduction and action in plant stress response, growth and development. *Ann. Bot.* **100**, 681–697.
- Wasternack, C. and Hause, B. (2013) Jasmonates: biosynthesis, perception, signal transduction and action in plant stress response, growth and development. An update to the 2007 review in *Annals of Botany*. *Ann. Bot.* **111**, 1021–1058.
- Yamaya-Ito, H., Shimoda, Y., Hakoyama, T., Sato, S., Kaneko, T., Hossain, M.S., Shibata, S., Kawaguchi, M., Hayashi, M. and Kouchi, H. (2017) Loss-of-function of ASPARTIC PEPTIDASE NODULE-INDUCED 1 (APN1) in *Lotus japonicus* restricts efficient nitrogen-fixing symbiosis with specific Mesorhizobium loti strains. *Plant J.* **93**, 5–16.
- Ye, H., Gemperline, E., Venkateshwaran, M., Chen, R., Delaux, P.M., Howes-Podoll, M., Ané, J.M. and Li, L. (2013) MALDI mass spectrometry-assisted molecular imaging of metabolites during nitrogen fixation in the *Medicago truncatula*-*Sinorhizobium meliloti* symbiosis. *Plant J.* **75**, 130–145.
- Zdyb, A., Demchenko, K., Heumann, J., Mrosk, C., Grzeganeck, P., Göbel, C., Feussner, I., Pawlowski, K. and Hause, B. (2011) Jasmonate biosynthesis in legume and actinorhizal nodules. *New Phytol.* **189**, 568–579.
- Zhang, N., Venkateshwaran, M., Boersma, M., Harms, A., Howes-Podoll, M., den Os, D., Ané, J.-M. and Sussman, M.R. (2012) Metabolomic profiling reveals suppression of oxylipin biosynthesis during the early stages of legume-rhizobia symbiosis. *FEBS Lett.* **586**, 3150–3158.

Metabolomic profiling of wild-type and mutant soybean root nodules using laser-ablation electrospray ionization mass spectrometry reveals altered metabolism

Beverly J. Agtuca¹, Sylwia A. Stopka², Sterling Evans¹, Laith Samarah², Yang Liu³, Dong Xu³,
Minviluz G. Stacey¹, David W. Koppenaal⁴, Ljiljana Paša-Tolić⁴, Christopher R. Anderton⁴,
Akos Vertes² and Gary Stacey^{1,*}

¹ Divisions of Plant Sciences and Biochemistry, Christopher S. Bond Life Sciences Center,
University of Missouri, Columbia, MO 65211, USA

² Department of Chemistry, The George Washington University, Washington, DC 20052, USA

³ Department of Electrical Engineering and Computer Science, Informatics Institute and
Christopher S. Bond Life Sciences Center, University of Missouri-Columbia, MO 65211, USA

⁴ Environmental Molecular Sciences Laboratory, Earth and Biological Sciences Directorate,
Pacific Northwest National Laboratory, 902 Battelle Boulevard, Richland, Washington 99354,
USA

*Author for correspondence:

Tel: +01 5738844752; E-mail: staceyg@missouri.edu

Dr. Gary Stacey

Curators' Distinguished Professor

Divisions of Plant Sciences and Biochemistry

271E Christopher S. Bond Life Sciences Center

University of Missouri, Columbia, MO 65211

Running Title (46/50 characters): LAESI-MS of wild-type and mutant soybean root nodules

SUPPORTING INFORMATION: Figures

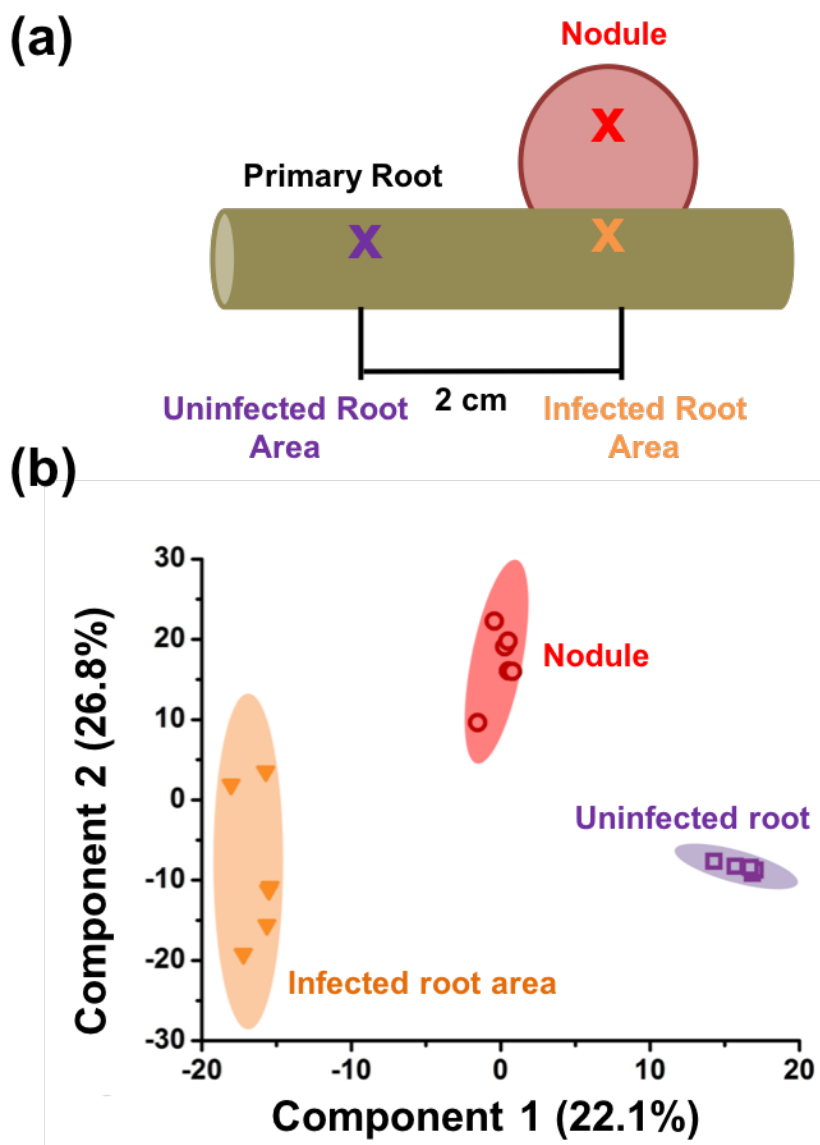


Figure S1. Metabolite profiling of soybean root anatomy when infected by WT *B. japonicum* using LAESI-MS in negative ion mode. (a) Schematic showing locations of ablation spots for LAESI-MS analysis (nodule, infected root area, and uninfected root area). (b) PLS-DA score plot showing the separation of sample types for the nodule in red, the infected root area in orange, and uninfected root area in purple.

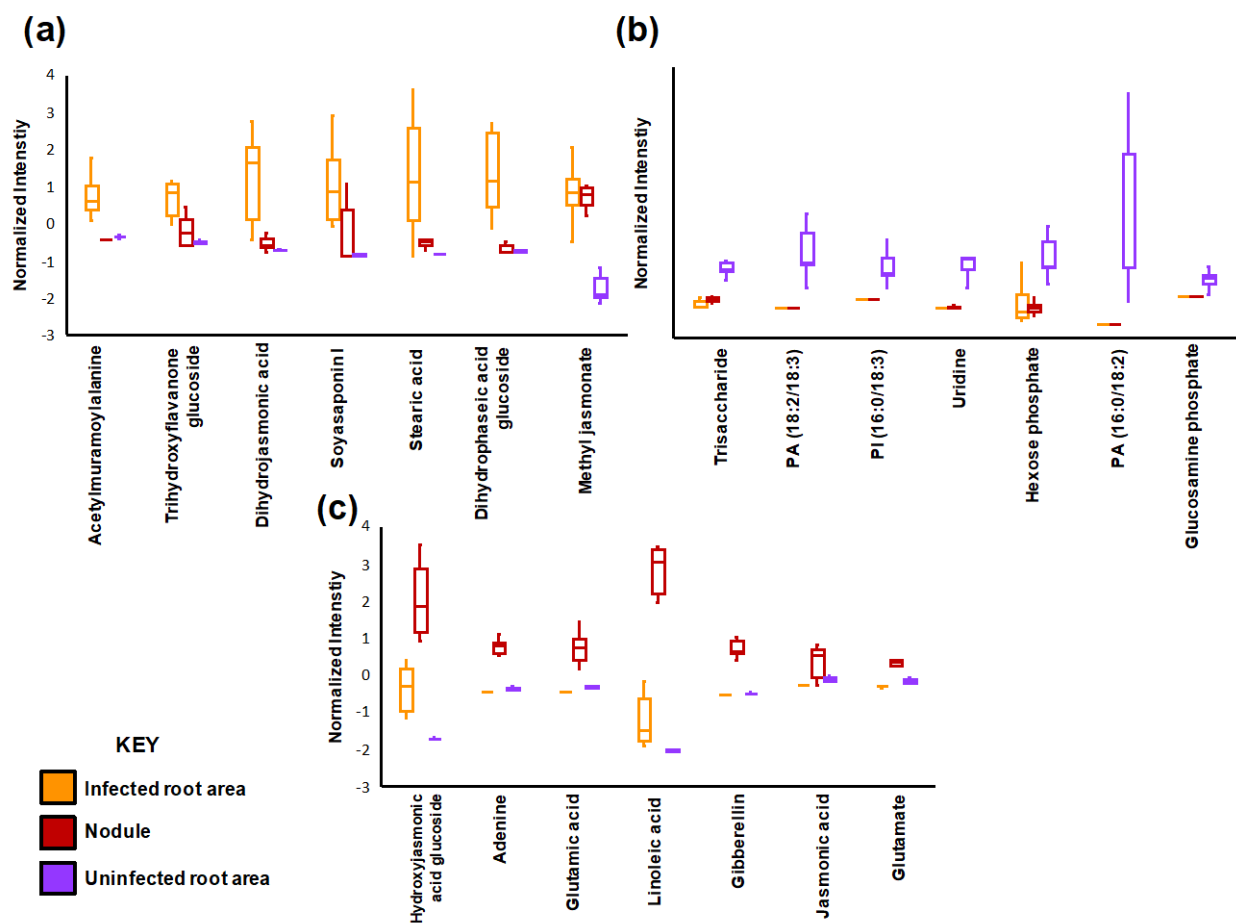


Figure S2. Box and whisker plots of significant metabolites that were highly abundant in the different areas of the primary root from negative ion mode. (a) Infected root area shown in orange, (b) uninfected root area shown in purple, and (c) the nodule shown in red. These metabolite abundances had fold change values $FC \geq 2$ and $p < 0.05$.

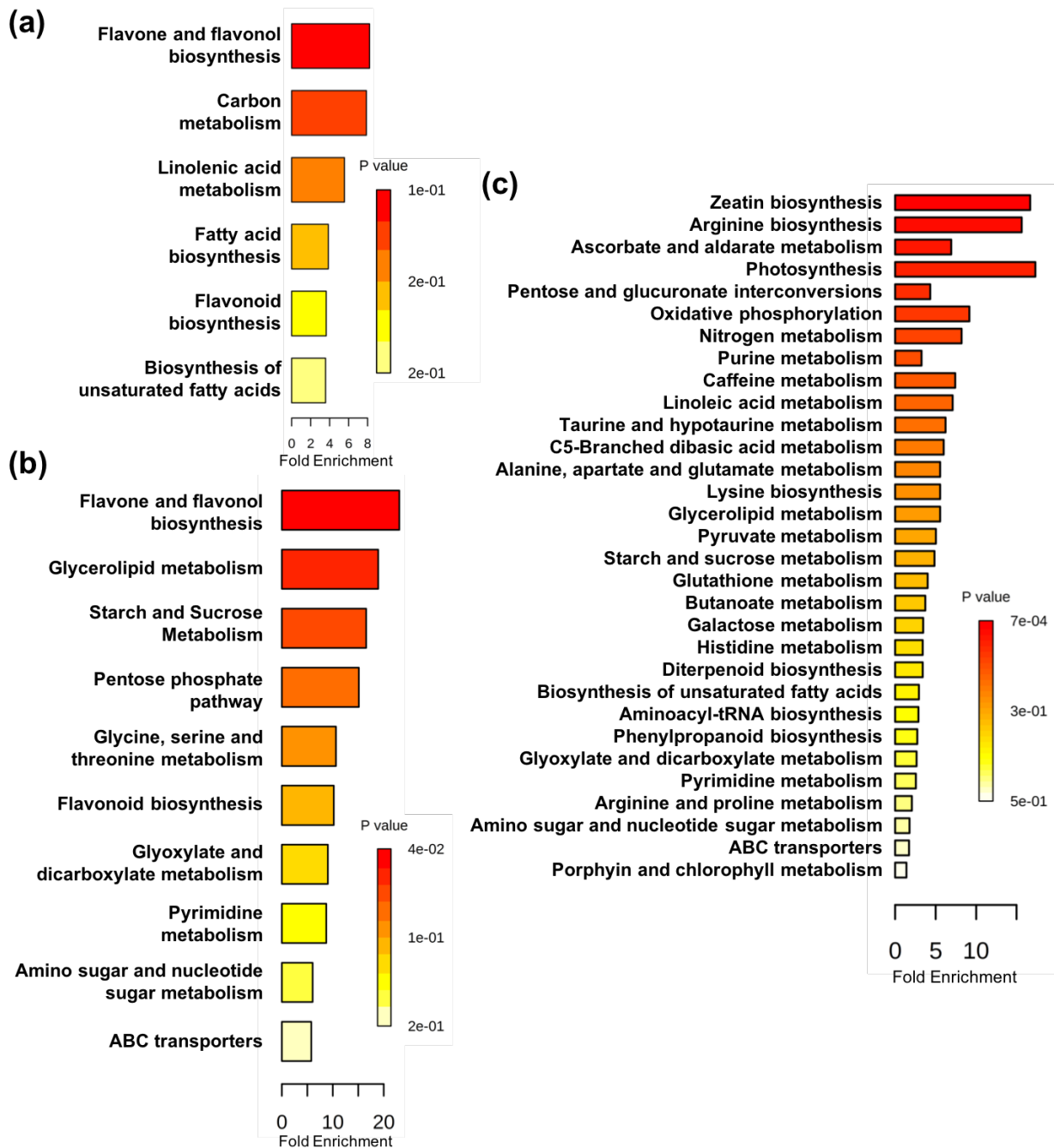


Figure S3. Fold enrichments represented by bar lengths for pathways highly affected in soybean primary roots by WT *B. japonicum* infection. Results are based on $n = 6$ areas analyzed of (a) the infected root, (b) the uninfected root, and (c) the nodule. The p-values are represented by false color scale ranging from statistically significant pathways in red to less significant pathways in yellow.

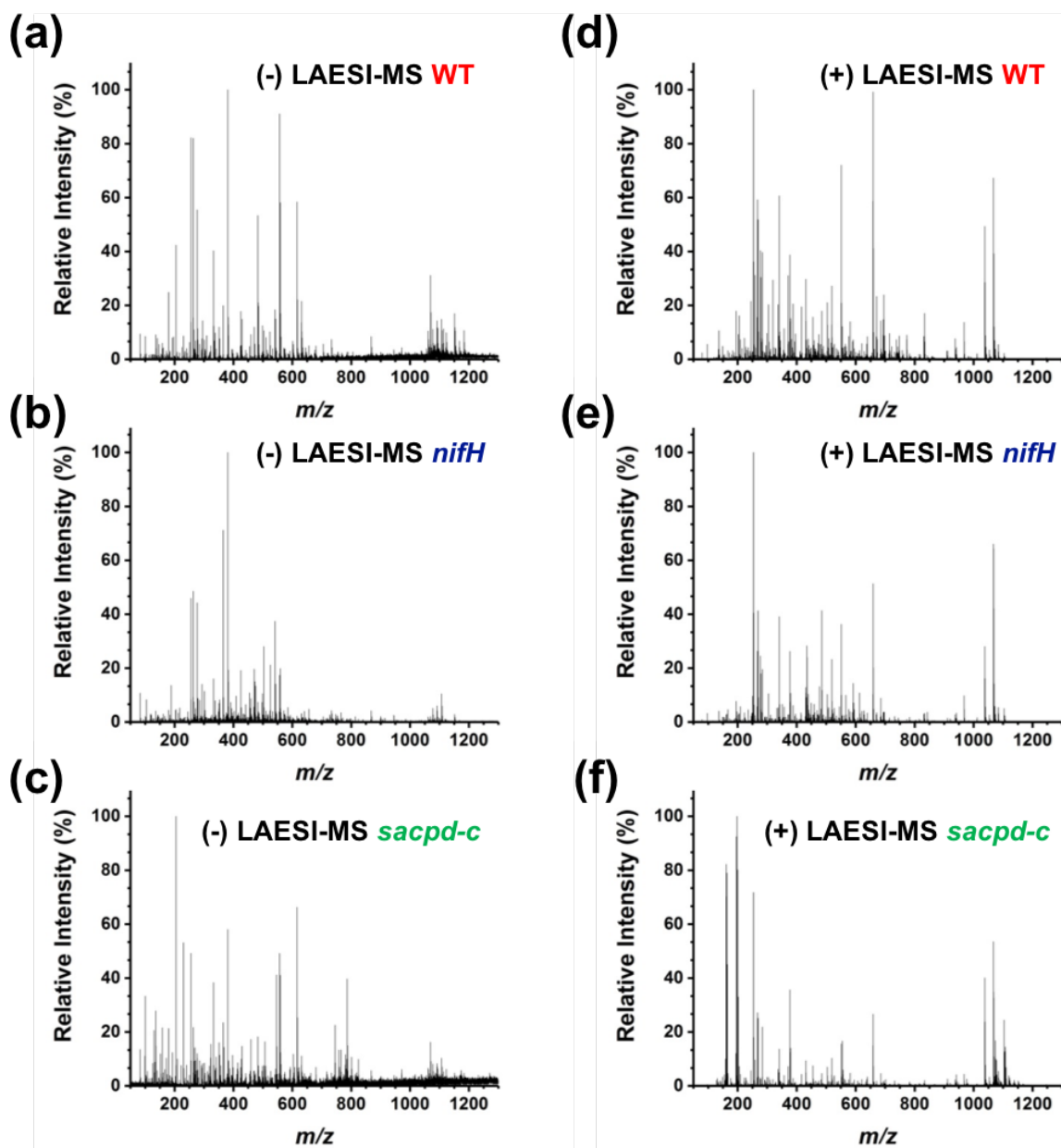


Figure S4. Mass spectra from LAESI-MS. Negative (a-c) and positive ion mode (d-f) mass spectra of root nodules resulting from infection by either *B. japonicum* WT (a and d) or *nifH* mutant (b and e), or nodules formed on the roots of *sacpd-c* mutant plants infected by *B. japonicum* WT (c and f).

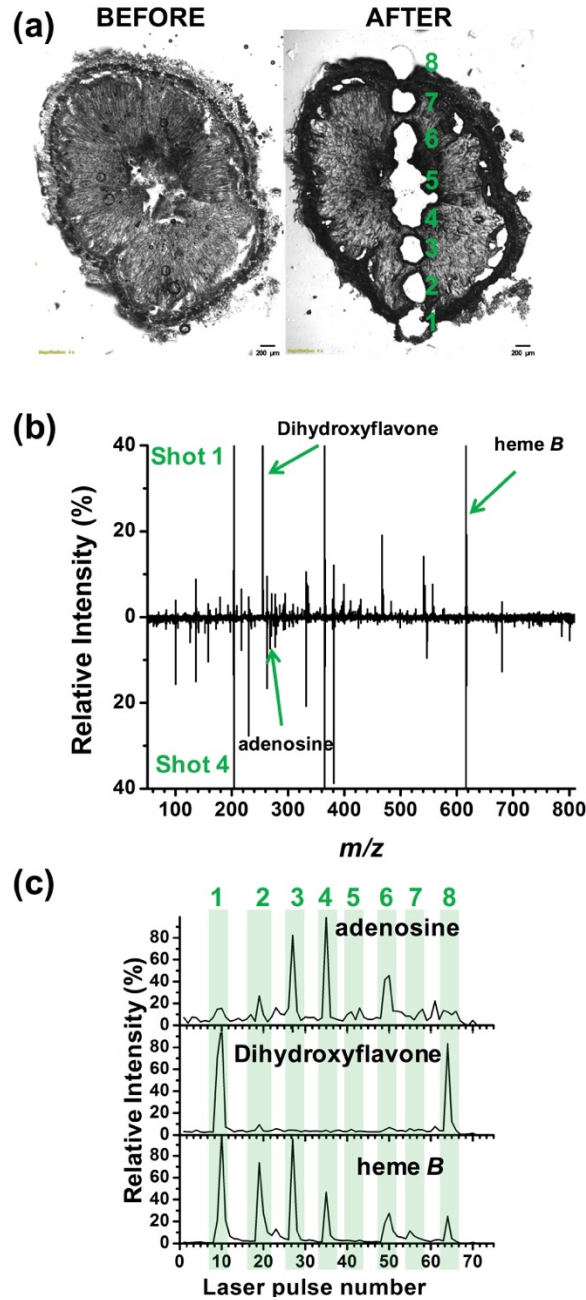


Figure S5. Comparison of metabolite profiles for 60 μm nodule sections derived from *sacpd-c* mutant plants in positive ion mode. (a) Bright field images before and after profiling by ablations at 8 positions in *sacpd-c*. Scale bars = 200 μm . (b) Comparison of average mass spectra from position 1 in the outer layer and position 4 in the necrotic lesion region. (c) Intensities of adenosine at $m/z= 268.117$, an uncharacterized metabolite at $m/z = 546.480$, dihydroxyflavone at $m/z= 255.068$, and heme *B* at $m/z= 616.178$ as a function of the number of laser pulses.

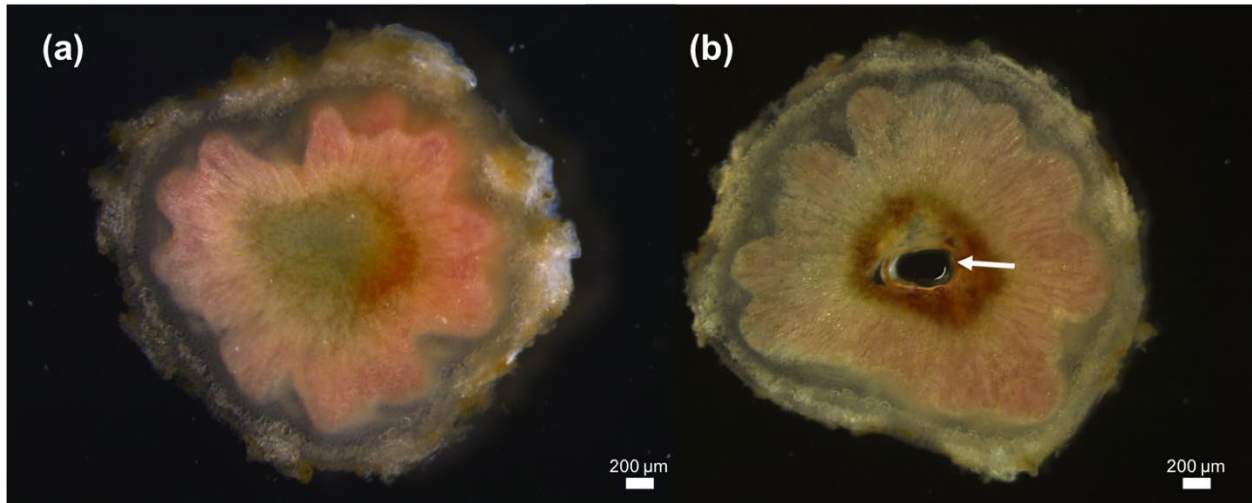


Figure S6. Microscopy images of nodule ultrastructure from mutant plant line *sacpd-c*. Nodules harvested at (a) 3 weeks after inoculation and (b) 4 weeks after inoculation. Arrow indicates the central Necrotic Zone (NZ). These nodules were sectioned at 100 μm . Scale bars = 200 μm .

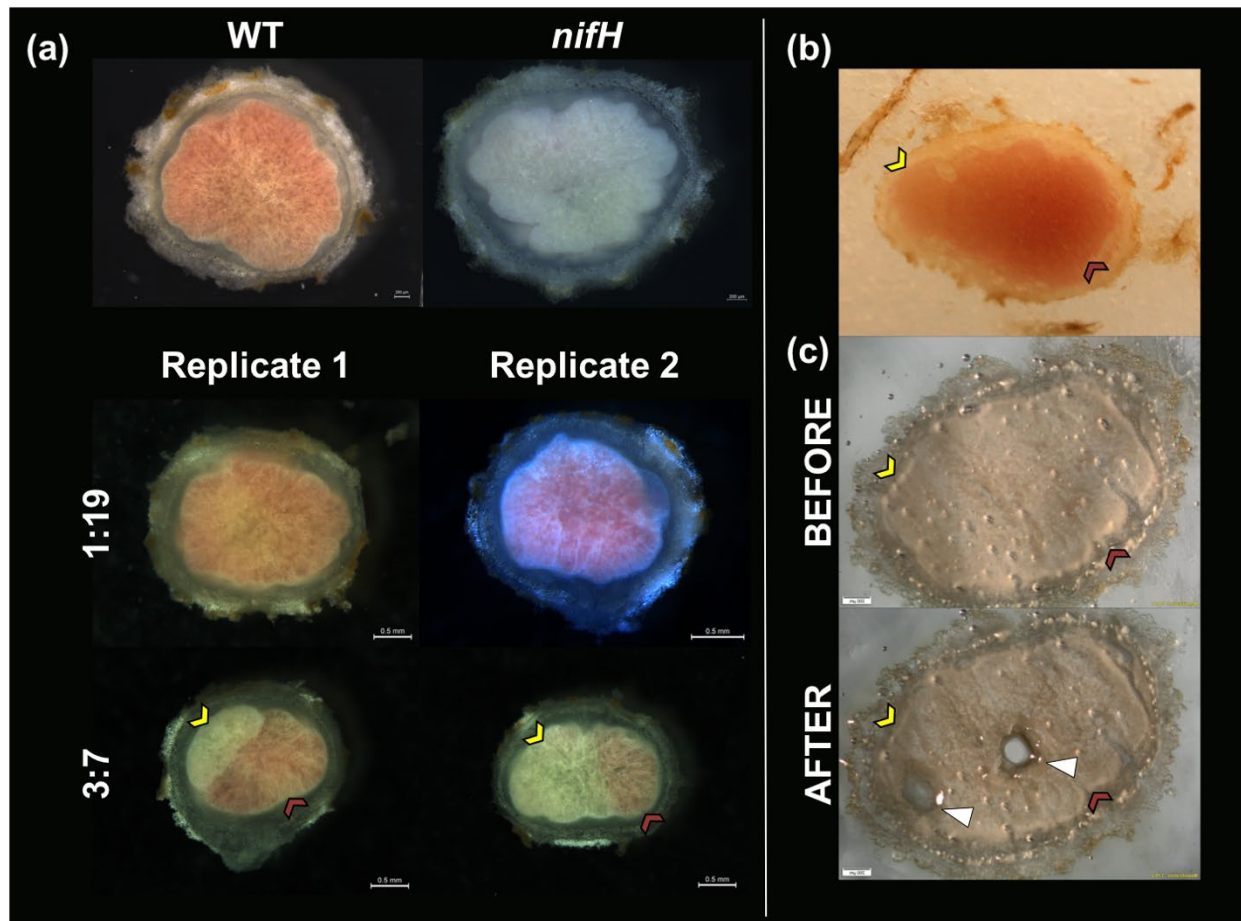


Figure S7. Phenotypic screening of co-inoculated nodules at different rhizobia inoculum ratios. (a) Comparison of sectioned nodules from plants that were infected by WT *B. japonicum*, *nifH* mutant strain, and mixed inoculums of 1:19 and 3:7, with images of replicates for the latter two. The 3:7 WT:*nifH* co-inoculated nodules showed the best phenotype of sectors. (b) An optical image of a CI nodule that was embedded with CMC and was placed on a stage in the cryostat. This image helped determine where the different sectors were pre-LAESI-MS analyses. (c) Before and after images of a LAESI-MS analyzed 3:7 co-inoculated nodule. The after image illustrates where the LAESI-MS ablation occurred (white arrows) in the distinctive sectors, where the ablation spot size was ~300 μm . Yellow arrows represent the ineffective endosymbionts shown in white and darker contrast, while white arrows display the effective endosymbionts shown in red/pink and a lighter contrast. Scale bars represent 200 μm for the WT and *nifH* images and 0.5 mm for the co-inoculated nodule images.

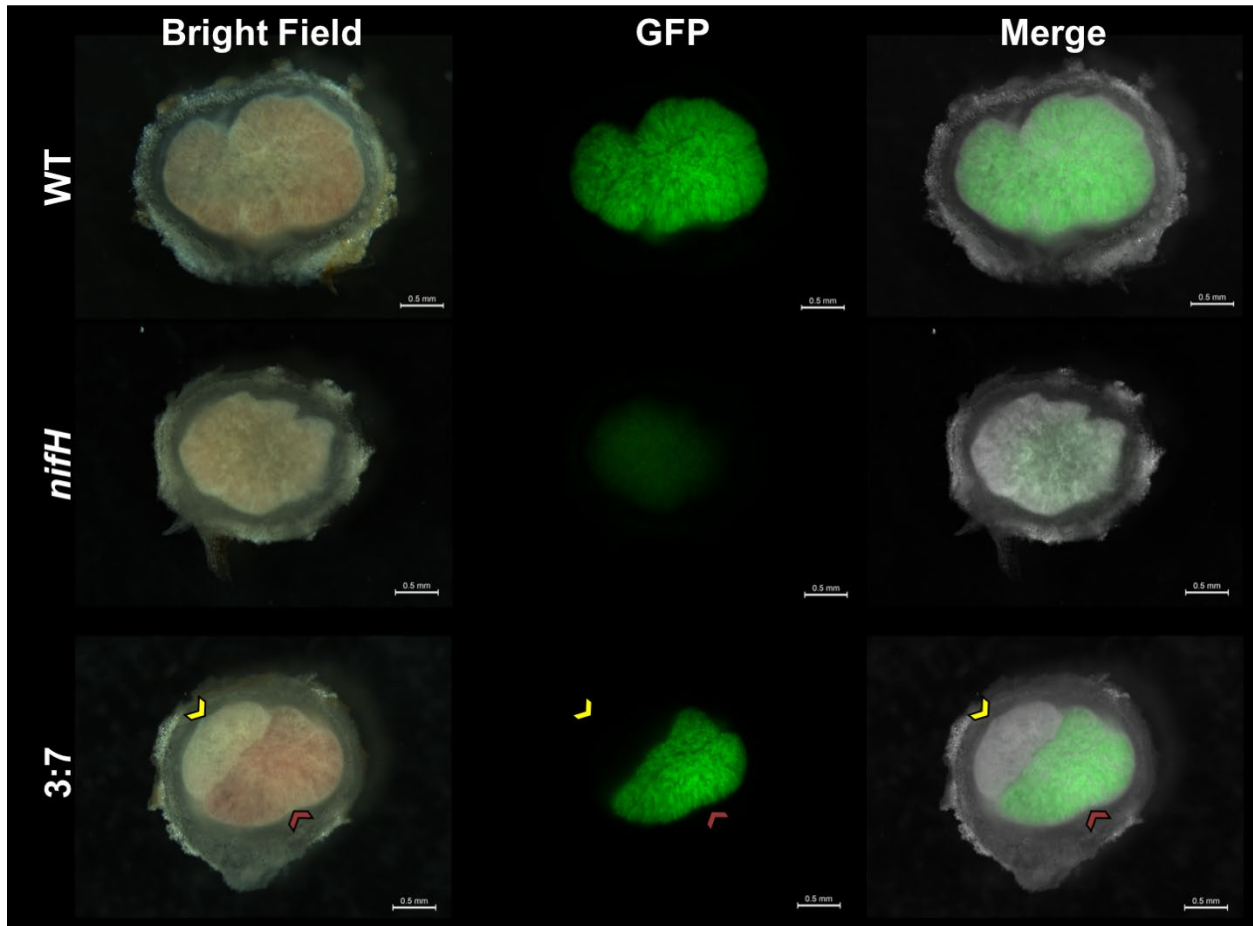


Figure S8. Fluorescence microscope images of *nifH* and 3:7 (WT:*nifH*) co-inoculated nodules. The first, second, and third columns illustrate the brightfield, fluorescence, and combined images, respectively. The WT *B. japonicum* is encoded with a GFP-label, whereas the *nifH* is not.

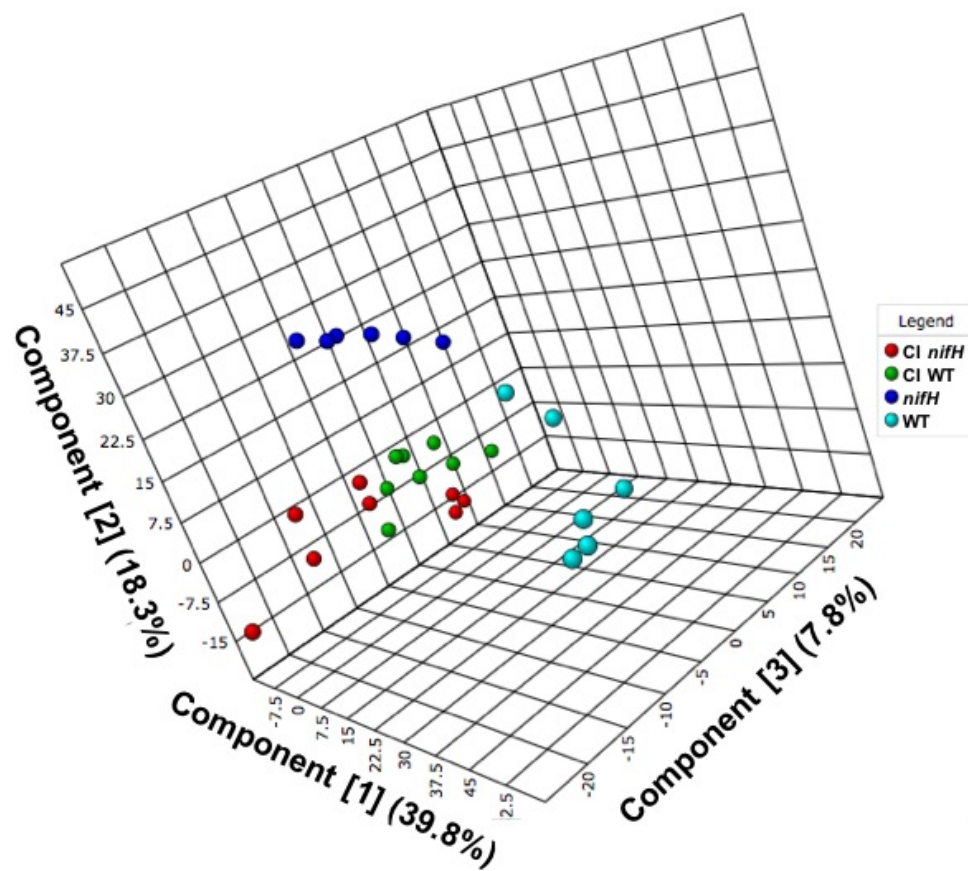


Figure S9. 3D PLS-DA score plot contrasting LAESI-MS data of WT, *nifH*, and co-inoculated nodules. Analyzed nodules were: infected by WT *B. japonicum* (light blue), *nifH* mutant strain (darker blue), and co-inoculated by 3:7 WT:*nifH* with a CI WT sector (green) and CI *nifH* sector (red).

SUPPORTING INFORMATION: Tables

Table S1. List of identified and unknown peaks that were highly abundant in the different areas of the WT primary root based on Figures S1-S3. The different root areas that were analyzed include the infected root area, uninfected root area, and nodule. These metabolites were significant by ANOVA with a f-value range of 4 to 282. (see excel spreadsheet)

Table S2. List of metabolites relating to Figure 1 with significant fold changes in the *sacpd-c* and *nifH* compared to the WT with a FC, of ≥ 2 and $p < 0.05$. Ion intensities for *nifH* and *sacpd-c* samples, I_{nifH} and $I_{sacpd-c}$, respectively, were compared to ion intensities for WT samples, I_{WT} .

Category	Compound	Kegg ID	Formula	MSI level ^e	log ₂ (FC) ^f	p value ^g
FC = $I_{sacpd-c}/I_{WT}$	Gluconic acid ^{a, c, -}	C00257	C ₆ H ₁₂ O ₇	2	1.01	5.76E-03
	Dihydroxyisoflavone ^{a, c, -}	C14344	C ₁₅ H ₁₀ O ₄	2	2.87	4.84E-03
	Trihydroxyflavone ^{a, b, -}	C01477	C ₁₅ H ₁₀ O ₅	1	4.43	3.00E-02
	PG(16:0/18:0) ^{c, -}		C ₄₀ H ₇₉ O ₁₀ P	2	4.72	4.87E-03
	PI(18:0/18:3) ^{c, -}		C ₄₅ H ₈₁ O ₁₃ P	2	1.94	2.82E-03
	PI(18:0/18:2) ^{c, -}		C ₄₅ H ₈₃ O ₁₃ P	2	2.77	1.66E-03
	Dehydrosoyasaponin I ^{a, c, -}	C08962	C ₄₈ H ₇₆ O ₁₈	2	3.04	3.37E-03
	Soyasaponin I ^{a, b, -}	C08983	C ₄₈ H ₇₈ O ₁₈	1	3.83	2.31E-05
	Trihydroxy-tetramethoxyflavone glycoside ^{a, -}		C ₂₅ H ₂₈ O ₁₄	3	2.07	5.37E-04
	Glucarate ^{a, -}	C00879	C ₆ H ₁₀ O ₈	3	1.37	2.35E-02
	Dihydroxyisoflavone ^{a, c, -}	C10208	C ₁₅ H ₁₀ O ₄	2	2.87	4.84E-03
	Glutamate ^{c, -}	C00025	C ₅ H ₈ NO ₄	2	-1.04	1.56E-03
	Acetyl-Glutamic acid ^{a, c, -}	C03871	C ₇ H ₁₁ NO ₅	2	-1.00	3.03E-03

	Methylcitrate/Homoisocitrate ^{a, -}	C01251	C ₇ H ₁₀ O ₇	3	-1.48	3.02E-05
	PA(16:0/18:1) ^{c, -}	C00416	C ₃₇ H ₇₁ O ₈ P	2	-6.72	1.42E-04
	PA(18:2/18:2) ^{c, -}		C ₃₉ H ₆₉ O ₈ P	2	-1.13	4.10E-03
	PE(16:0/18:2) ^{c, -}	C00350	C ₃₉ H ₇₄ NO ₈ P	2	-1.99	4.19E-07
	PE(16:0/18:1) ^{c, -}	C13877	C ₃₉ H ₇₆ NO ₈ P	2	-1.99	4.19E-07
	PE(18:1/18:2) ^{c, -}	C00157	C ₄₁ H ₇₅ NO ₈ P	2	-2.85	9.04E-03
	PG(16:0/18:2) ^{c, -}		C ₄₀ H ₇₅ O ₁₀	2	-1.72	1.02E-03
	PG(16:0/18:1) ^{c, -}	C13883	C ₄₀ H ₇₇ O ₁₀ P	2	-1.76	1.02E-03
	PI(16:0/18:2) ^{c, -}		C ₄₃ H ₇₉ O ₁₃ P	2	-1.43	5.61E-05
	Cyclohexylamine ^{c, +}	C00571	C ₆ H ₁₃ N	2	-1.58	1.19E-06
	Glucosylpyridoxine ^{a, c, +}	C03996	C ₁₄ H ₂₁ NO ₈	2	-1.52	1.44E-07
	Adenosylmethionine ^{a, c, +}	C00019	C ₁₅ H ₂₂ N ₆ O ₅ S	2	-1.62	1.22E-04
FC = I_{nifH}/I_{WT}	Methylcitrate/Homoisocitrate ^{a, -}	C01251	C ₇ H ₁₀ O ₇	3	-1.37	4.09E-04
	Coumesterol ^{a, c, -}	C10205	C ₁₅ H ₈ O ₅	2	-2.31	1.00E-03
	Butene tricarboxylate ^{a, -}	C16579	C ₇ H ₈ O ₆	3	-2.81	6.74E-05
	Hydroxyoctadecatrienoic acid ^{a, c, -}	C16316	C ₁₈ H ₃₀ O ₃	2	-4.76	3.08E-02
	Epoxyoctadecenoic acid ^{a, c, -}	C08368	C ₁₈ H ₃₂ O ₃	2	-4.76	3.08E-02
	Disaccharide ^{a, c, -}	C00208	C ₁₂ H ₂₂ O ₁₁	2	4.37	2.50E-02
	Adenine ^{b, -}	C00147	C ₅ H ₅ N ₅	1	-1.47	2.13E-03
	Pentose ^{c, -}	C00181	C ₅ H ₁₀ O ₅	2	-1.45	1.20E-03
	Acetyl-Glutamic acid ^{a, c, -}	C03871	C ₇ H ₁₁ NO ₅	2	-3.45	2.45E-04
Gluconic acid ^{a, c, -}	C00514	C ₆ H ₁₂ O ₇	2	-1.13	9.78E-05	

Heme B ^{a, c, +}	C00032	C ₃₄ H ₃₂ FeN ₄ O ₄	2	-3.70	4.43E-02
Hexose phosphate ^{a, c, -}	C01097	C ₆ H ₁₃ O ₉ P	2	-1.04	3.57E-03
Gibberellin ^{b, -}	C01699	C ₁₉ H ₂₂ O ₆	1	-1.28	3.52E-02
Benzoyloxyhydroxypropyl glucopyranosiduronic acid ^{c, -}		C ₁₆ H ₂₀ O ₁₀	2	-2.36	2.77E-05
Dihydroxyisoflavone malonyl glycoside ^{c, -}	C16191	C ₂₄ H ₂₂ O ₁₂	2	-2.11	9.72E-03
Hydroxy-dimethoxyflavone glycoside ^{c, -}		C ₂₃ H ₂₄ O ₁₀	2	-5.16	1.95E-03
Hydroxyjasmonic acid glycoside/Tuberonic acid glycoside ^{a, c, -}	C08558	C ₁₈ H ₂₈ O ₉	2	-1.29	1.30E-03
PG(18:1/18:1) ^{c, -}	C00344	C ₄₂ H ₇₉ O ₁₀ P	2	-2.51	1.74E-03
PI(16:0/18:2) ^{c, -}		C ₄₅ H ₇₈ O ₁₃ P	2	-1.95	4.00E-04
UDP-hexose ^{a, -}	C00029	C ₁₅ H ₂₄ N ₂ O ₁₇ P ₂	3	-2.41	2.11E-02
Jasmonic acid ^{a, c, -}	C08491	C ₁₂ H ₁₈ O ₃	2	4.57	1.47E-08
Hydroxyjasmonic acid ^{a, -}	C21385	C ₁₂ H ₁₈ O ₄	3	3.29	6.33E-04
Dihydrojasmonic acid ^{a, c, -}	C16309	C ₁₂ H ₂₀ O ₃	2	1.93	1.93E-03
Methyl jasmonate ^{a, -}	C11512	C ₁₃ H ₂₀ O ₃	3	1.48	2.34E-02
Hydroperoxyoctadecadienoic acid ^{a, c, -}	C07338	C ₁₈ H ₃₂ O ₄	2	2.38	3.30E-02
Oxooctadecatrienoic acid ^{a, c, -}	C16320	C ₁₈ H ₂₈ O ₃	2	2.41	1.17E-04
Epoxyoctadecadienoic acid ^{a, c, -}	C16316	C ₁₈ H ₃₀ O ₃	2	2.49	2.80E-04
Epoxyoctadecenoic acid ^{a, c, -}	C08368	C ₁₈ H ₃₂ O ₃	2	2.44	2.80E-04

Heptose ^{a, -}	C02076	C ₇ H ₁₄ O ₇	3	1.74	2.21E-02
Glycosyl glycerol-phosphate ^{a, c, -}	C01225	C ₉ H ₁₉ O ₁₁ P	2	4.29	6.35E-05
Tryptophan ^{a, c, -}	C00078	C ₁₁ H ₁₂ N ₂ O ₂	2	5.25	3.87E-02
Tetrahydroxyflavanone glycoside ^{a, c, -}	C16408	C ₂₁ H ₂₂ O ₁₁	2	1.30	1.45E-02
Dihydrochalcone glycoside ^{a, -}	C01604	C ₂₁ H ₂₄ O ₁₀	3	2.15	4.05E-02
Isoflavone glycoside ^{a, -}	C12625	C ₂₅ H ₂₄ O ₁₃	3	3.30	2.68E-02
Dihydroxymethoxyflavanone diglycoside ^{a, -}	C09806	C ₂₈ H ₃₄ O ₁₅	3	2.40	3.94E-03
Trihydroxyflavanone glycoside ^{a, -}	C09789	C ₂₇ H ₃₂ O ₁₄	3	2.98	6.31E-03
Dihydroxyflavone glycoside ^{a, c, -}	C10216	C ₂₁ H ₂₀ O ₉	2	1.51	5.08E-04
Hydroxyflavanone glycoside ^{a, c, -}	C16989	C ₂₁ H ₂₂ O ₉	2	3.88	7.88E-03

^a Compounds assigned based on ultra-high mass accuracy of 21 T FT-ICR.

^b Compounds assigned based on in-house tandem MS of standards performed under identical conditions.

^c Compounds assigned based on tandem MS databases comparisons (<http://metlin.scripps.edu> and NIST/EPA/NIH Mass Spectral Library Version 2.2).

^d CCS values obtained from our in-house CCS LAESI-IMS-MS library.

^e Metabolomics Standards Initiative (MSI) levels of identification: Level 1 necessitates that 2 or more orthogonal properties of a chemical standard (here, measured mass of the compound and its tandem MS) analyzed in a laboratory are compared to experimental data acquired in the same laboratory with the same analytical methods. Level 2 requires that 2 or more orthogonal

properties of a compound (here, also measured mass of the compound and its tandem MS) are compared with external reported literature values. Level 3 annotation is based on comparison of the compound's measured m/z with the calculated value.

^f The fold change is the ratio of the intensity of a given compound in the *nifH*- or *sacpd-c* lesion area to the intensity of the same ion in the *wt* group. The cutoff value for the fold change is 2.

^g The threshold for the p-value is 0.05.

+ Positive Ion Mode

- Negative Ion Mode

Table S3. List of identified and unknown compounds relating to Figure 1 in negative and positive ion mode datasets. The species that are in bold are significant with a fold change of FC = > 2 and p-value <0.05 when comparing WT nodules (positively up-regulated) and mutant nodules (negatively down-regulated), *nifH* and *sacpd-c*. (see excel spreadsheet)

Table S4. List of compounds relating to Figure 3 with significant fold changes in the infection zone and outer layer when comparing nodules formed by either *B. japonicum* WT or *nifH* mutant strain. These species had a significant fold change, FC = > 2 and p-value <0.05. (see excel spreadsheet)

Table S5. Annotated metabolites that were significantly different between nodule types. The rest of the annotated metabolites in 60 µm thick sections of nodules infected by either *B. japonicum* wild-type, the *nifH* mutant strain, or co-inoculated by both strains. The nodules that were inoculated with both strains showed two distinctive sectors: the co-inoculated WT (CI W) sector and the co-inoculated *nifH* (CI N) sector. These species have a significant fold change, FC, of at least two and p-value < 0.05 shown in bold based on MSI of metabolite identification.

Compound	KEGG ID	Log ₂ (FC)						f.value	Fisher's LSD
		WT vs. <i>nifH</i>	WT vs. CW	WT vs. CN	<i>nifH</i> vs. CW	<i>nifH</i> vs. CN	CW vs. CN		

Acetylcarnitine/ Isopentenyladenine ^{d, f, g, +}	C04083	3.04**	7.81*	6.50**	4.83**	4.12**	0	76.95**	WT > CN; WT > CW; WT > <i>nifH</i>
N-benzoyl-L-glutamate ^{h, +}	NA	-1.47**	0	0	4.04**	2.92**	0	74.21**	<i>nifH</i> > CN; <i>nifH</i> > CW; <i>nifH</i> > WT
Linoleic acid ^{d, -}	C01595	-0.39**	3.06**	3.02**	3.47**	3.44**	7.02	67.43**	<i>nifH</i> > CN; WT > CN; <i>nifH</i> > CW; WT > CW; <i>nifH</i> > WT
Trihydroxy- tetramethoxyflavone glucoside ^{a, -}	NA	3.58**	6.84**	2.59**	-4.81	-4.56*	0.90	48.91**	WT > CN; WT > CW; WT > <i>nifH</i> ; CN > <i>nifH</i>
Acetylcarnitine ^{g, -}	C02571	3.36**	6.10**	4.74**	0	0	0	45.53**	WT > CN; WT > CW; WT > <i>nifH</i>
Glycosyl glycerol- phosphate ^{a, c, -}	C01225	-4.30**	0.57	0.14	4.97**	4.62**	-0.37	37.47**	<i>nifH</i> > CN; <i>nifH</i> > CW; <i>nifH</i> > WT
Glutamyl-iso/leucine ^{g, -}	NA	1.57**	3.26**	4.63**	-2.44*	-1.33	1.53	37.45**	WT > CN; WT > CW; WT > <i>nifH</i> ; CW > <i>nifH</i>
N-Feruloylglycine ^{e, g, -}	C02564	-3.33**	0	0	5.20**	4.61**	0	30.10**	<i>nifH</i> > CN; <i>nifH</i> > CW; <i>nifH</i> > WT <i>nifH</i> > CN; CN > WT; <i>nifH</i> > CW; CW > WT; <i>nifH</i> > WT
Turanose ^{f, +}	NA	-2.81**	-2.19**	-1.25	0.67**	0.62**	0.03	26.50**	<i>nifH</i> > WT
Acetyl-Glutamic acid ^{a, c, f, -}	C03871	2.83**	3.65**	3.43**	0	0	0	26.01**	WT > CN; WT > CW; WT > <i>nifH</i>
Trihydroxyoctadecenoic acid ^{a, -}	C14833	3.86**	3.34**	4.66**	0	0	0	25.89**	WT > CN; WT > CW; WT > <i>nifH</i>
Benzoyloxyhydroxypropyl glucopyranosiduronic acid ^{c, -}	NA	4.5**	2.11**	2.69**	-2.58*	-2.35	0.46	23.93**	WT > CN; WT > CW; WT > <i>nifH</i> ; CW > <i>nifH</i>
Disaccharide ^{d, -}	C00089	-1.86**	1.26*	0.49	3.06**	2.31**	-1.62	23.63**	<i>nifH</i> > CN; <i>nifH</i> > CW; <i>nifH</i> > WT
Hydroxyflavanone glucoside ^{a, c, -}	C16989	3.65**	3.37**	3.71**	0	0	0	19.87**	WT > CN; WT > CW; WT > <i>nifH</i>
Coumesterol ^{a, c, f, -}	C10205	2.31**	2.69**	2.78**	0.07	0	0.37	17.56**	WT > CN; WT > CW; WT > <i>nifH</i>
Epoxyoctadecenoic acid ^{a, c, -}	C08368	-2.49**	-0.21	0.1	2.30**	2.64**	0.58	17.36**	<i>nifH</i> > CN; <i>nifH</i> > CW; <i>nifH</i> > WT
Theophylline ^{d, +}	C07130	1.73*	2.49**	1.86**	0.852*	0.41	-0.32	17.26**	WT > CN; WT > CW; WT > <i>nifH</i>
Coniceine ^{e, +}	NA	3.91**	2.47**	1.75**	-1.56*	-2.16	-0.49	16.14**	WT > CN; WT > CW; WT > <i>nifH</i>
Trihydroxy octadecenoic acid ^{f, +}	C1483								
	3	-1.99*	0	0	4.11**	2.44**	0	14.03**	<i>nifH</i> > CN; <i>nifH</i> > CW; <i>nifH</i> > WT
Acetyl glutamic acid ^{d, +}	C00624	-5.15	-4.55**	-4.89**	-6.34**	-6.48**	-1.30**	13.94**	CN > CW; CN > <i>nifH</i> ; CN > WT; CW > <i>nifH</i> ; CW > WT

Heptose ^{a, -}	C02076	-3.02*	-0.67	3.98**	2.53**	4.10**	1.85	13.74**	<i>nifH</i> > CN; <i>nifH</i> > CW; <i>nifH</i> > WT; WT > CN
Hydroxyoctadecatrienoic acid ^{a, c, -}	C16316	-1.87**	-0.18	0.32	1.70**	2.24**	0.76	12.13**	<i>nifH</i> > CN; <i>nifH</i> > CW; <i>nifH</i> > WT
Heme B ^{a, c, +}	C00032	3.61*	7.9512**	0.03	-2.93*	-1.93	1.39*	11.04**	WT > CW; WT > <i>nifH</i> ; CW > CN; WT > CN
Adenine ^{d, +}	C00147	3.16**	1.53**	3.82*	-1.79*	-2.48*	-0.57	10.70**	CN > <i>nifH</i> ; WT > CN; WT > CW; WT > <i>nifH</i>
Aminooctanoic acid/citrulline ^{d, +}	C00327	1.46	-2.47**	-2.63*	-4.26**	-4.11**	-0.55	9.27**	CN > <i>nifH</i> ; CN > WT; CW > <i>nifH</i> ; CW > WT
PA(38:2) ^{e, -}	NA	3.84**	2.76**	2.88**	0	0	0	9.15**	WT > CN; WT > CW; WT > <i>nifH</i>
Allantoin ^{d, +}	C01551	0.25*	-3.49**	-2.91**	-5.28**	-4.63**	-0.05	9.11**	CN > <i>nifH</i> ; CN > WT; CW > <i>nifH</i> ; CW > WT; WT > <i>nifH</i>
Gluconic acid ^{a, c, g, -}	C00257	2.48**	-1.54*	-0.74	-4.29**	-3.80**	1.21*	9.00**	CW > CN; CW > <i>nifH</i> ; CW > WT; CN > <i>nifH</i> ; WT > <i>nifH</i>
Homostachydrine/Lentiginosine ^{e, +}	NA	3.99*	4.48*	1.66	0	0	0	8.70**	WT > CW; WT > <i>nifH</i> ; WT > CN
Hydroxy-dimethoxyflavone glucoside ^{c, -}	NA	-2.96*	-0.83	0	1.98*	3.46**	1.21	8.58**	<i>nifH</i> > CN; <i>nifH</i> > CW; <i>nifH</i> > WT
Vanillic acid ^{d, -}	C06672	0	-2.75*	-1.18	-2.89*	-1.32	2.68*	8.55**	CW > CN; CW > <i>nifH</i> ; CW > WT
Curcumin ^{h, +}	NA	-1.63*	0	0	3.12*	3.05**	0	8.13**	<i>nifH</i> > CN; <i>nifH</i> > CW; <i>nifH</i> > WT
Isoflavonoid ^{g, +}	NA	-2.57**	-4.97**	-4.14**	1.20*	1.50**	0.36	7.70**	<i>nifH</i> > CN; > <i>nifH</i> > CW; <i>nifH</i> > WT; CW > WT; CN > <i>nifH</i>
Hydroxy methoxyisoflavone ^{d, +}	NA	7.35*	-6.68**	-6.66	-8.47**	-7.73*	-0.09	7.61**	CN > <i>nifH</i> ; CN > WT; CW > <i>nifH</i> ; CW > WT; WT > <i>nifH</i>
PG(16:0/18:1) ^{c, -}	C13883	2.83**	2.15**	1.07*	-0.76	-1.79	-1.07	7.09**	WT > CN; WT > CW; WT > <i>nifH</i>
Pyranosylhexose ^{g, -}	NA	0	4.17**	1.98*	0	0	0	6.59**	WT > CN; WT > CW
Galactopinitol ^{g, -}	NA	1.20*	4.38**	1.72*	-1.62	0	2.27*	6.58**	WT > CN; WT > CW; WT > <i>nifH</i> ; CW > CN
Pentose ^{c, -}	C00216	1.45**	-3.23*	-3.1*	-3.37*	-3.26*	0.89	6.46**	CW > <i>nifH</i> ; CW > WT; CN > <i>nifH</i> ; CN > WT; WT > <i>nifH</i>
Pinoresinol glucoside ^{f, +}	NA	0.90	-1.53*	0	-3.32**	0	1.12*	6.31**	CW > CN; CW > <i>nifH</i> ; CW > WT
Succinylornithine ^{g, +}	C03415	-1.74	-4.48**	-4.13*	-1.78*	-1.58	0.31	6.17**	CN > WT; CW > <i>nifH</i> ; CW > WT
S-adenosyl methionine ^{a, c, d, e, +}	C00019	1.40*	-0.24	-3.51*	-5.62**	-5.28*	-0.37	5.97**	CN > <i>nifH</i> ; CN > WT; CW > <i>nifH</i> ; CW > WT; WT > <i>nifH</i>
Nicotinamide ^{h, +}	NA	1.27	-1.47*	0	-3.26**	0	0.18	5.72**	CW > <i>nifH</i> ; CW > WT
Hydrolyzable tannin ^{g, +}	NA	0	-2.8**	-2.57*	-4.59**	-4.18*	-0.52	5.71**	CN > <i>nifH</i> ; CN > WT; CW > <i>nifH</i> ; CW > WT

Phosphocholine ^{d, +}	C00588	0.08	-4.03**	-3.08**	-3.09*	-2.80*	0.32	5.65**	CN > <i>nifH</i> ; CN > WT; CW > <i>nifH</i> ; CW > WT
Trihydroxyflavanone glucoside ^{d, -}	C09099	-2.07*	-1.71	1.89**	0.51	1.04	1.80*	5.63**	CW > CN; WT > CN; <i>nifH</i> > WT; <i>nifH</i> > CN; CW > WT
Hexotriose ^{d, g, +}	C01835	5.46**	4.87*	3.31*	-0.62	-1.05	-0.31	5.28*	WT > CN; WT > CW; WT > <i>nifH</i>
Adenosine ^{h, +}	NA	-1.44	-1.88*	-1.91*	-3.67**	-3.45*	-0.44	4.98*	CN > <i>nifH</i> ; CN > WT; CW > <i>nifH</i>
Tetrahydroxyflavone glucoside ^{d, +}	NA	4.22*	-1.32*	0	-3.11**	0	0.46	4.75*	CN > <i>nifH</i> ; CW > <i>nifH</i> ; CW > WT; WT > <i>nifH</i>
Glucosylpyridoxine ^{a, c, f, +}	C03996	0.29	1.98*	1.73*	1.78*	1.80**	0.74	4.62*	<i>nifH</i> > CN; WT > CN; <i>nifH</i> > CW; WT > CW
PC(36:2) ^{e, +}	NA	4.05*	6.86*	4.61*	0	0	0	4.24*	WT > CN; WT > CW; WT > <i>nifH</i>
Daidzin ^{g, +}	C10216	-3.42	0	-2.83	0	-4.28	-1.84	4.08*	CN > CW; CN > <i>nifH</i> ; CN > WT
Sucrose-phosphate ^{e, +}	C16688	5.31**	-1.99	0	-3.78*	0	0.42	3.97*	CN > <i>nifH</i> ; CW > <i>nifH</i> ; CW > WT; WT > <i>nifH</i>
Nicotianamine ^{g, +}	C05324	0	-2.65*	-2.60*	-4.44*	-4.14*	-0.37	3.79*	CN > <i>nifH</i> ; CN > WT; CW > <i>nifH</i> ; CW > WT

- ^a Compounds assigned based on ultra-high mass accuracy of 21 T FT-ICR.
- ^b Compounds assigned based on in-house tandem MS of standards performed under identical conditions.
- ^c Compounds assigned based on tandem MS databases comparisons (<http://metlin.scripps.edu> and NIST/EPA/NIH Mass Spectral Library Version 2.2).
- ^d Compounds assigned in Stopka *et al.* 2017
- ^e Compounds assigned in Veličković *et al.* 2018
- ^f Compounds assigned in Stopka *et al.* 2019
- ^g Compounds from Laith *et al.* 2020 accepted
- + Positive Ion Mode
- Negative Ion Mode
- *P < 0.05 and **P < 0.005

Metabolomic profiling of wild-type and mutant soybean root nodules using laser-ablation electrospray ionization mass spectrometry reveals altered metabolism

Beverly J. Agtuca¹, Sylwia A. Stopka², Sterling Evans¹, Laith Samarah², Yang Liu³, Dong Xu³,
Minviluz G. Stacey¹, David W. Koppenaal⁴, Ljiljana Paša-Tolić⁴, Christopher R. Anderton⁴,
Akos Vertes² and Gary Stacey^{1,*}

¹ Divisions of Plant Sciences and Biochemistry, Christopher S. Bond Life Sciences Center,
University of Missouri, Columbia, MO 65211, USA

² Department of Chemistry, The George Washington University, Washington, DC 20052, USA

³ Department of Electrical Engineering and Computer Science, Informatics Institute and
Christopher S. Bond Life Sciences Center, University of Missouri-Columbia, MO 65211, USA

⁴ Environmental Molecular Sciences Laboratory, Earth and Biological Sciences Directorate,
Pacific Northwest National Laboratory, 902 Battelle Boulevard, Richland, Washington 99354,
USA

*Author for correspondence:

Tel: +01 5738844752; E-mail: staceyg@missouri.edu

Dr. Gary Stacey

Curators' Distinguished Professor

Divisions of Plant Sciences and Biochemistry

271E Christopher S. Bond Life Sciences Center

University of Missouri, Columbia, MO 65211

Running Title (46/50 characters): LAESI-MS of wild-type and mutant soybean root nodules

SUPPORTING INFORMATION: Experimental Procedures

Methods S1. Bacterial growth conditions.

Bradyrhizobium japonicum USDA110 wild-type strain (WT) was from our (Stacey) laboratory collection, whereas the *B. japonicum* *fix*-mutant H1 (*nifH*) strain, derived from USDA110, was generously provided by Dr. Hans-Martin Fischer (Hahn et al., 1984). Bacterial cells were grown for 2 d at 30°C in HM medium (Cole and Elkan, 1973) (HEPES, 1.3 g L⁻¹; MES, 1.1 g L⁻¹; Na₂HPO₄, 0.125 g L⁻¹; Na₂SO₄, 0.25 g L⁻¹; NH₄Cl, 0.32 g L⁻¹; MgSO₄•7H₂O, 0.18 g L⁻¹; FeCl₃, 0.004 g L⁻¹; CaCl₂•2H₂O, 0.013 g L⁻¹; yeast extract, 0.25 g L⁻¹; D-Ara, 1 g L⁻¹; sodium gluconate, 1 g L⁻¹; and pH 6.6). The medium for the WT was supplemented with 25 mg L⁻¹ of tetracycline and 100 mg L⁻¹ of spectinomycin, while that for the growth of the *nifH* mutant was supplemented with 100 mg L⁻¹ of spectinomycin and kanamycin. The bacterial culture reached OD₆₀₀=0.8 (10⁸ cells ml⁻¹). Then, the culture was centrifuged at 3,000 rpm for 10 min, washed 3x with sterile water. This culture solution was then used as seedling inoculation.

Methods S2. Nodules that were infected by mix-inoculums

Three-week-old nodules, co-inoculated with *B. japonicum* WT that expressed green fluorescent protein and *nifH* mutant at ratios of 3:7 and 1:19 (Regus et al., 2017), were sectioned at 100 µm using a Vibratome 3000 Plus and imaged by a stereomicroscope (M205 FA, Leica, Illinois, U.S.). The phenotype of nodules from different inoculum ratios was analyzed to distinguish the white and red sectors, as well as the GFP expression from the *fix*⁺ rhizobia. The 3:7 ratio nodules showed the best sector resolution and, hence, were used for analysis. These nodules and their attached roots were harvested, frozen in liquid nitrogen, and stored at -80°C until LAESI-MS analysis. The nodules were cryosectioned at 60 µm thickness and were imaged by a Canon EOS REBEL T6 DSLR to indicate the directionality of the sectors. Next, the thaw-mounted samples were imaged by an upright microscope (IX71, Olympus, Tokyo, Japan) before and after LAESI-MS analysis to determine where the ablated sample areas were relative to the individual sectors.

Methods S3. Instrumentation for LAESI-MS.

The LAESI-MS instrumentation was similar to our previous work (Stopka et al., 2017). A homebuilt LAESI ion source was retrofitted on the front of a quadrupole time-of-flight mass spectrometer equipped with traveling wave ion mobility separation (Synapt G2S, Waters, Milford, MA). The laser component consisted of an optical parametric oscillator driven Nd:YAG laser (IR

Opolette HE 2731, Opotek, Carlsbad, CA) that produced 7 ns laser pulses at 2.94 μm with the repetition rate in the 1-20 Hz range. The laser beam was steered through a 30 mm cage system and a 75 mm focal length plano-convex ZnSe lens (Infrared Optical Products, Farmingdale, NY) with its focal spot on the sample. A homebuilt Peltier stage was constructed and implemented in the analysis to maintain a temperature of 0°C to reduce sample drying. Following the ablation, a plume of neutrals is formed and expands into an electrospray oriented perpendicular to the expansion direction and on axis with the MS orifice. Both positive and negative ion modes were utilized, with emitter (MT320-50-5-5, New Objective, Woburn, MA) voltages and ESI solution compositions of +3.3 kV and 1:1 (v/v) MeOH:H₂O with 0.1% acetic acid for positive ion mode, and -2.7 kV with 2:1 (v/v) mixture of MeOH:CHCl₃ for negative ion mode. The IMS parameters were set to 90 mL/min flow rate and 3.35 bar pressure for the nitrogen drift gas, 1.41 V for the delay coefficient, and 40 V for the height and 650 m/s for the velocity of the traveling wave.

Methods S4. Data and pathway analysis.

All root segments, nodules, and free-living rhizobia had a minimum of six biological replicates for LAESI-MS analysis. The data analysis for univariate, multivariate, and hierarchical clustering statistical approaches were done using MetaboAnalyst 4.0, as previously described in the supporting information of Stopka et al. (2017). The data was normalized (summing the spectral intensities for each sample and then the Pareto scaling was done by using the square root of standard deviation as the scaling factor.

Metabolite pathway enrichment was conducted using MetaboAnalyst 4.0 at <http://www.metaboanalyst.ca>. We downloaded 133 soybean pathways from KEGG as our metabolite set library and the metabolite sets that contained at least two compounds. KEGG compound names were converted to HMDB compound names by mapping HMDB IDs.

Methods S5. Sample preparation for tandem electrospray ionization mass spectrometry (ESI-MS/MS).

Approximately 0.25 g of either WT, *nifH*, or *sacpd-c* soybean root nodules stored at -80°C were gently plucked with sterile forceps and transferred to a pre-chilled mortar. The nodules were ground with a pestle in liquid nitrogen until a fine powder was obtained. For identification of metabolites in positive ion mode, 2 mL of 1:1 (v/v) methanol:water with 0.1 % acetic acid solution were added to the mortar. The mixture was homogenized and then transferred to a 2 mL Eppendorf tube. For negative ion mode, the powdered tissue was homogenized in 2:1 (v/v)

chloroform:methanol. The tubes were centrifuged at 5000×g for 5 min at 4°C and the supernatant was transferred to new 2 mL Eppendorf tubes and stored at -80°C for analysis by ESI-MS/MS.

Methods S6. Tandem electrospray ionization mass spectrometry (ESI-MS/MS).

The prepared lysate was transferred from Eppendorf tubes stored at -80°C to a 500 µL Hamilton syringe. The syringe was secured on a syringe pump and connected to a stainless steel emitter (MT320-50-5-5, New Objective, Woburn, MA) through a fused silica tube. The flow rate was set at 500 nL/min and the solution was sprayed by applying a voltage to the emitter at + 3300 V for positive ion mode and -2200 V for negative ion mode. The generated ions were introduced into a Q-ToF mass spectrometer (Synapt G2S, Waters, Milford, MA) and the ions of interest from the spectra obtained previously by LAESI-MS were selected for tandem MS by collision induced dissociation (CID). Collision energies were ramped from 50 eV.

Methods S7. Metabolite identification.

The Metabolite Standard Initiative (MSI) level of metabolite identification was adopted for peak assignments. Three different properties were used for peak assignments: (i) accurate mass, (ii) tandem MS comparisons with one of three databases, <http://metlin.scripps.edu>, NIST/EPA/NIH Mass Spectral Library Version 2.2, or our in-house collection of tandem mass spectra of standards measured under identical conditions, and (iii) CCS comparisons with either a database (Paglia et al., 2014) or an in-house CCS library acquired by LAESI-IMS-MS.

The in house LAESI-IMS-MS library is based on our CCS and tandem MS measurements for a collection of 618 small metabolites (Mass Spectrometry Metabolite Library of Standards, MSMLS, IROA Technologies, Bolton, MA) described at <https://www.sigmaaldrich.com/content/dam/sigma-aldrich/docs/Sigma/Datasheet/10/msmlsdat.pdf>.